The evolutionary status of the short-period cataclysmic variable BW Scl

Iikka Mäntynen

March 24, 2021

Contents

1 Abstract **3**

2 Introduction **4**

3 Classifications **4**
3.1 CV Classification 4
3.2 Dwarf Nova Classification 5

4 Components of CVs **6**
4.1 Secondary Star 6
4.1.1 Roche-Lobe Overflow 7
4.2 Gas Stream 7
4.3 Accretion Disc 7
4.4 Bright Spot 10
4.5 Primary Star 11

5 Observing Dwarf Novae **12**
5.1 Photometry in Quiescence 12
5.2 Spectroscopy in Quiescence 13
5.3 Photometry in Outburst 17
5.4 Spectroscopy in Outburst 18

6 Disc Instability Model **19**
6.1 Theory 19
6.2 Effect on Outburst Morphology 21

7 CV Evolution **22**
7.1 Stability of Mass-Transfer 22
7.2 Response to the Mass Loss 23
7.3 Angular Momentum Loss 24
7.3.1 Magnetic Braking 24
7.3.2 Gravitational Radiation 24
7.4 Period Gap 25
7.5 Period-Minimum and Period-Bouncers 26

8 BW Sculptoris **27**

9 Observations **28**
9.1 EFOSC2 28
9.2 X-shooter 29

9.3 UVES 29

10 Data Reduction **30**
10.1 EFOSC2 30
10.2 X-shooter and UVES 30

11 Overview of Spectral Features in BW Scl **31**

12 The Radial Velocity Curve **34**
12.1 Double Gaussian Method 34
12.2 Results 36

13 Determination of Orbital Parameters **40**
13.1 Mg II line absorption 40
13.2 White Dwarf Mass 40
13.3 Mass-ratio and Secondary Mass 41
13.4 Semi-Major Axis and Radial Velocity 41

14 Accretion Disc Parameters **41**

15 Doppler Tomography **46**
15.1 Overview 46
15.2 Profile Projection 47
15.3 Maximum Entropy Inversion 47
15.4 Doppler maps of BW Scl 48

16 Direct Measurements of the Secondary **50**
16.1 Hα Emission 50
16.2 The "K-correction" 51
16.3 Calcium Emission 51

17 Conclusion **53**

18 Acknowledgements **54**

Appendix A **58**

1 Abstract

This Master's thesis is dedicated to studying an accreting white dwarf system, namely BW Sculptoris, which is long considered to be one of the best candidates for so-called period-bouncers. In the accreting white dwarfs, also known as cataclysmic variable stars (CVs), the donor component is a low mass main-sequence star or a brown dwarf which loses matter via the inner Lagrangian point. According to standard evolutionary theory, cataclysmic variables evolve from longer to shorter orbital periods. Theory of CV evolution predicts that the secondary star eventually loses enough mass for transforming into a brown dwarf, after that the orbital period starts increasing again. Such post-period-minimum systems are called "period-bouncers". The standard model predicts more than half of the cataclysmic variables should be at the post-period-minimum stage. However, the period-bouncers are observed far below the rates predicted by the theory. Thus the primary aim of this study is to determine whether the secondary star in BW Scl is a brown dwarf. Data for this research is collected from European Southern Observatory archives and utilizes data from the following instruments and telescopes: EFOSC2 (ESO NTT), X-shooter (ESO VLT) and UVES (ESO VLT). Methods of analysis include radial velocity analysis, emission line profile modelling, and Doppler tomography. Our study has determined the secondary star mass M2 $= 0.066 \pm 0.013\ M_{\odot}$, below the hydrogen-burning minimum mass limit of 0.075 $M_{\odot}$. Combining it with the near period-minimum orbital period , we come to the conclusion that BW Scl is a period-bouncer.

2 Introduction

Cataclysmic variables (CVs) are interacting binaries, where the primary is a white dwarf, and the secondary is a low mass main-sequence star or a brown dwarf. The secondary fills its Roche-lobe due to evolutionary effects and starts losing mass through the inner Lagrangian point. If the primary is not strongly magnetic, the transferred material forms an accretion disc, and is eventually accreted by the primary (Warner 1995).

The theory of CV evolution predicts that the periods of CVs evolve from longer to shorter periods. Eventually at a period-minimum, the secondaries evolve into sub-stellar brown dwarfs, at which point the orbital periods start increasing instead of decreasing. CVs with brown dwarf secondaries are known as "period-bouncers". BW Sculptoris was recognised as a good candidate for a period-bouncer by Patterson (2011) and thus the primary aim of this thesis is to determine whether the secondary in BW Scl is a main sequence star or a brown dwarf.

This thesis utilizes data from multiple European Southern Observatory (ESO) telescopes and instruments: EFOSC2 (ESO NTT), X-shooter (ESO VLT), UVES (ESO VLT) and also utilizes data from AAVSO. The methods of choice for data analysis include Doppler tomography, radial velocity analysis and emission profile modelling. Since the binary components are not resolved, spectroscopic data is required to model the nature of the components.

3 Classifications

3.1 CV Classification

CVs are historically classified in the following way (Warner 1995; Hellier 2001):

- Classical Novae (CNe) are objects which have had only one observed eruption. The eruption is caused by a runaway thermonuclear process on the surface of the primary.
- Recurrent Novae (RNe) are previously recognized CNs that are found to repeat their eruptions.
- Dwarf Novae (DNe) have weaker outbursts than CN and RN. The outburst is caused by sudden increase of mass transfer rate through the accretion disc, and the subsequent increase in release of gravitational potential energy.

- Nova-like Variables (NLs) include all the 'non-eruptive' CVs.
- Magnetic CVs, which have strong magnetic fields that disrupt the infalling material's path

3.2 Dwarf Nova Classification

DNe are characterized by outbursts separated by periods of quiescence. In quiescence usually only small, sometimes rapid brightness fluctuations are observed. In outburst the brightness of the object rises rapidly by several magnitudes. The brightness then gradually returns to original level on much longer time frame compared to the initial rise. Intervals between outbursts can vary from days to years. Intervals between consecutive outbursts for a given object may vary, but each object is characterized by a specific mean interval length. Longer intervals between outbursts are associated with larger amplitude outbursts.

DNe are divided to three subtypes based on the morphology of their outburst light curve (Warner 1995; Hellier 2001):

- Z Cam objects show prolonged standstills approximately 0.7 mag below outburst brightness, which may last from tens of days to years. The standstills occur always on the declining phase of the outburst.
- SU UMa objects have occasional superoutbursts which compared to normal outbursts are brighter by approximately 0.7 mag and last $\sim$5 times longer. Normal outbursts are similar to those of U Gem type. The superoutbursts exhibit superposed periodic oscillations (superhumps), with periods similar to the orbital period and magnitudes about 0.2-0.3 mag in visual.
- U Gem (SS Cyg in some sources) objects include all the DN that cannot be classified into the aforementioned subtypes.

The main three subtypes have sub-classifications, here we consider only WZ Sagittae since BW Scl is classified as such:

WZ Sge objects are a subclass of SU UMa. In this type the interval between super-outbursts is long (>4 years). This is because of a low mass-transfer rate. Normal outbursts are few or absent. They show double-waved early superhumps coincident with the orbital period at the beginning of their outbursts. They undergo re-brightenings. Orbital periods range from $\sim$72 to $\sim$115 min. Amplitudes are larger than $\sim$7 magnitudes (AAVSO 2019).

The white dwarfs in CVs can also be classified. In the case of BW Scl the classification is ZZ Ceti. These variables are non-radially pulsating white dwarfs that change their brightness with periods from 30 s to 25 min and amplitudes from 0.001 to 0.2 mag in the V band. They usually show several close period values. ZZ Ceti stars in CVs are also called GW Librae stars (AAVSO 2019).

4 Components of CVs

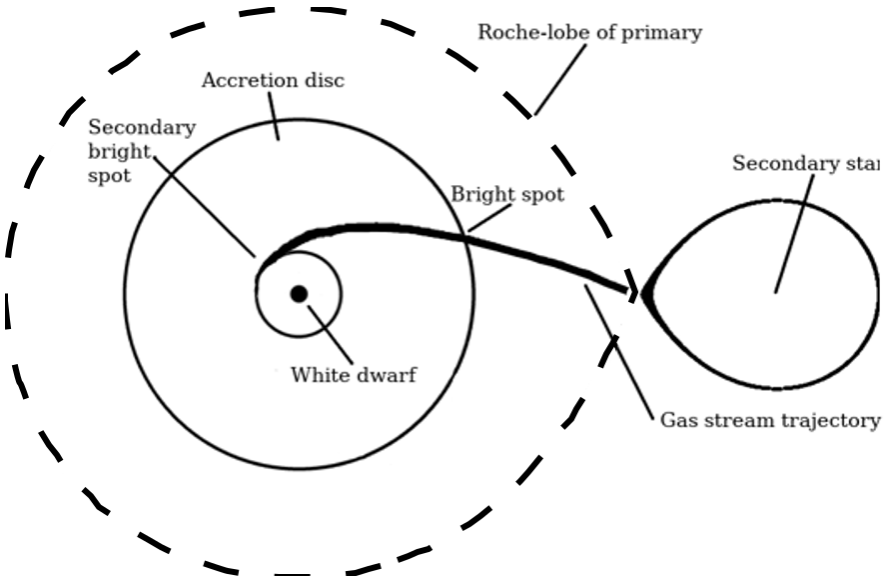

Figure 1: Schematic image of a CV system, looking face-on the orbital plane.

4.1 Secondary Star

Secondaries in DN are either a low mass main-sequence star or a substellar brown dwarf. Evolutionary effects cause them to fill their Roche-lobe, either by increase of the radius of the secondary due to nuclear evolution, or by shrinking of the semi-major axis of the orbit. There is not a one-to-one correspondence between secondaries in CVs and similar mass stars in isolation. Secondaries in CVs are somewhat larger and hotter, their shapes are distorted and distribution of radiation asymmetrical (Warner 1995; Hellier 2001).

4.1.1 Roche-Lobe Overflow

The shape of the secondary star is highly distorted when it fills or is about to fill its Roche-lobe. Shapes of the Roche equipotentials are given by equation 1, where G is the gravitational constant, M_1 and M_2 are masses of the primary and secondary respectively, $\mu_2 = M_2/(M_1+M_2)$ and P_{orb} is the orbital period. Coordinates are Cartesian and set up as follows: origin is at the primary, x-axis is towards the secondary, y-axis is to the direction of the orbital motion of the primary and z-axis is perpendicular to the orbital plane. Shapes of the Roche equipotentials are only a function of the mass fraction $q = M_2/M_1$, scaled by the semi-major axis, since the masses and P_{orb} are connected by Kepler's third law. Roche-lobe is the largest of these Roche equipotentials that can contain the star. The Roche-lobes of the stars connect at the inner Lagrangian point L_1, which is a saddle point of Φ. When the volume of the secondary star exceeds the volume of the Roche-lobe, material starts to fall to the primary through the inner Lagrangian point (Warner 1995; Hellier 2001).

$$\Phi = -\frac{GM_1}{(x^2+y^2+z^2)^{1/2}} - \frac{GM_2}{((x-a)^2+y^2+z^2)^{1/2}} - \frac{1}{2}\Big(\frac{2\pi}{P_{orb}}\Big)^2[(x-\mu_2 a)^2+y^2] \tag{1}$$

4.2 Gas Stream

At L_1 material is bound to neither of the stars and is co-rotating with the stars. Gas starts to fall at approximately thermal velocity of the atoms in the gas. Schematic view of the situation is in Figure 2.

Gas stream starts to quickly expand at local speed of sound while falling from L_1, thus pressure forces are quickly negligible. Trajectory of the gas stream follows that of single particles, and is deflected by the Coriolis effect. This causes the stream to miss the white dwarf due to its compactness. Interactions between the gas particles orbiting the primary dissipate the angular momentum over the material, forcing them on a circular orbits (Warner 1995; Hellier 2001).

4.3 Accretion Disc

The gas that is transferred from the secondary initially forms a ring around the white dwarf. Viscous shear between adjacent annuli causes most particles to drift inwards, and angular momentum conservation forces some particles to move outwards, a disc forms. At the first order approximation particles

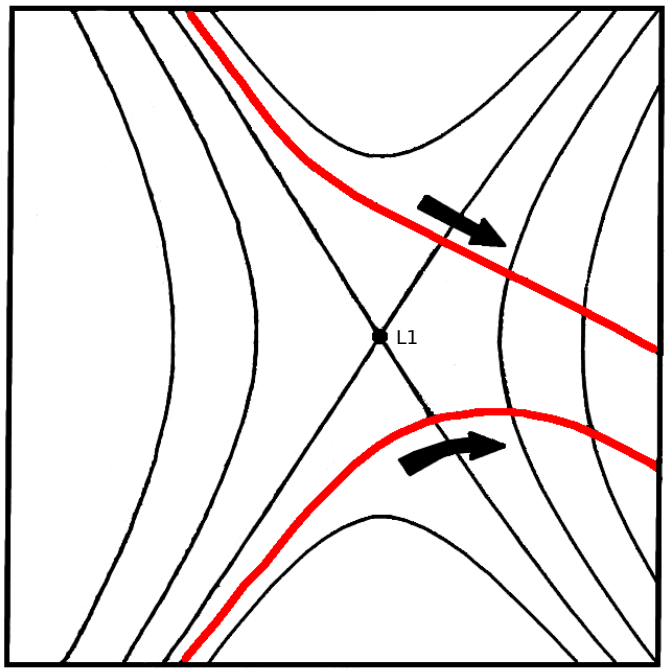

Figure 2: Schematic view of the gas flowing from the L1 towards the primary. Black lines mark Roche equipotentials, red lines mark surface of the secondary and the gas flow. Note that here the primary is to the right. Adapted from Pringle & Wade (1985).

move at Keplerian orbits, with a small inwards drift that is small compared to tangential velocity.

Inner parts of the accretion disc are not significantly affected by the tidal forces of the secondary. These forces become increasingly significant as we move towards the outer edge of the disc. If pressure and viscosity effects can be neglected, orbits of individual particles follow closely ones of the restricted three body problem. These orbits become increasingly quasi-elliptical at larger radii, until at certain radius, the orbits intersect. Resulting tidal shear will prevent the disc from extending much beyond this radius. This radius is approximated by equation 2 as a function of q, or more accurately in equation 3 by Neustroev & Zharikov (2020) for a low mass ratio.

$$\frac{r_d(max)}{a} = \frac{0.60}{1+q} \qquad 0.1 < q < 0.4 \tag{2}$$

$$\frac{r_d(max)}{a} = 0.353 + 0.271e^{-3.045q} \qquad 0.03 < q < 0.73 \tag{3}$$

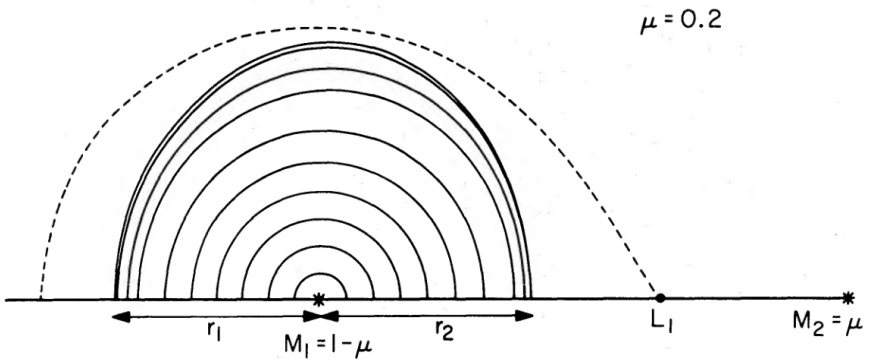

Figure 3: Orbits in accretion disc. Roche-lobe of the primary is marked with the dashed line. From Paczynski (1977).

Asymmetry in the accretion disc generates a torque between the disc and the secondary. This can be seen in the Figure 3. This allows angular momentum to be fed from the outer parts of the accretion disc back to the secondary.

At the inner edge of the accretion disc the material has the problem of settling on the surface of the white dwarf. Keplerian velocities at the inner disc radii are much faster than the usual rotational velocities of white dwarfs. Thus the material accreting onto the white dwarf needs to lose a large portion of its kinetic energy in order to settle on the surface. This region is called the boundary layer (BL). If the surface of the white dwarf is rotating well below the Keplerian velocity, the BL can be as luminous as the rest of the disc. The BL is radiating a lot of energy from a relatively small surface area, resulting to a high effective temperature. Optically thin BL radiates at hard x-rays, whereas optically thick radiates at soft x-rays and EUV. Outside the BL the effective temperature of a theoretical steady disc would follow relation in equation 4.

$$T_{eff}(r) \propto r^{-3/4} \tag{4}$$

The accretion disc isn't perfectly flat and has vertical structure. Density in vertical direction drops exponentially as we move further from the plane of the disc. Vertical scale height increases with the radius from the primary, making the faces of the accretion disc concave. This concave face can then be exposed to light from the primary and the BL, causing considerable heating on the disc.

Besides tidal limitation on the maximum size of the disc, the secondary has resonant effects on the disc. Resonances such like 2:1, 3:1 and 3:2 are

possible and can cause eccentricity in the disc. Depending on the mass ratio of the system, some of these resonances may fall outside the maximum extent of the disc and thus don't have an effect. If the resonances are present, the resulting eccentric orbits can then precess and produce observable phenomenon (Warner 1995; Frank et al. 1985).

4.4 Bright Spot

With the accretion disc fully formed, the gas stream impacts the outer edge of the disc at supersonic speeds. This impact region is shock-heated and may outshine all the other components. This region is called the bright spot, hot spot or hot line. The position of the bright spot is in the intersection of the free-fall trajectory of the gas stream and the outer edge of the disc. The predicted geometry of the bright spot is a function of only the mass ratio q, so the bright spot has been used to measure the size of the disc and the mass ratio.

There are few complications to this simplified picture though. First, if the impact region is optically thick, some material from the gas stream may bounce back from the bright spot and spray back to the Roche-lobe. Second, denser parts of the stream may penetrate deeper into the disc, locally heating it. This increases its local scale height, creating a bulge that rotates for some distance, typically half the perimeter. Third, two shocks may form, creating triangular shaped region. Fourth, part of the stream may flow over the disc, in so called stream overflow (Lubow & Shu 1976). This overflow follows single particle trajectory and then hits the inner edge of the disc at the other side, approximately at 148° from the direction of the secondary (Warner 1995; Hellier 2001).

4.5 Primary Star

The white dwarf primary in CVs is often not resolved due to its low luminosity compared to that of the disc and the bright spot. However, in several low mass-transfer and high inclination systems the eclipse of the white dwarf by the companion is visible. Additionally in some low mass-transfer systems the disc emission is weak enough that the white dwarf is visible, typically as broad absorption throughs at hydrogen Balmer lines.

Unlike white dwarfs in isolation, which are in constant cooling state, white dwarfs in CVs receive a supply of heat and mass from the BL. White dwarfs in CVs are on average hotter and more massive and thus smaller in radii compared to those in isolation (Pala & Gänsicke 2017). Shorter period CVs have tendency to have colder white dwarfs, evidently a result of shorter period CVs having lower mass-transfer rates.

Temperature of white dwarf in CVs is a result of multiple factors. Mass-transfer rate through the disc and the BL provides constant heating, counteracting the constant cooling. The accretional heating is greatly enhanced during outburst, when the mass-transfer rate through the disc is increased. Also an even greater heating effect comes from classical nova eruptions, when the accreted material burns in a runaway nuclear fusion.

Accretional heating is located on the equator, where the material lands on the surface. The material and heat then diffuses from there to other areas of the white dwarf. The equator is also more strongly irradiated by the bright BL (Warner 1995; Hellier 2001).

5 Observing Dwarf Novae

5.1 Photometry in Quiescence

DNe in quiescence show variations in brightness which have few sources: orbital motion, flickering from the bright spot, variations in the disc, and brightness variations of the white dwarf.

Effects of orbital motion range from eclipses, partial obstruction of components to almost no effect in face-on systems. Eclipses can be used to directly measure system parameters. Flickering from the bright spot is explained by the gas stream and the impact area varying in time. The disc can differ greatly from the stationary disc model. These include: eccentricities, precession, density waves, spirals and turbulent areas. Figure 4 shows a light curve of BW Scl exhibiting these variations. (Warner 1995; Hellier 2001)

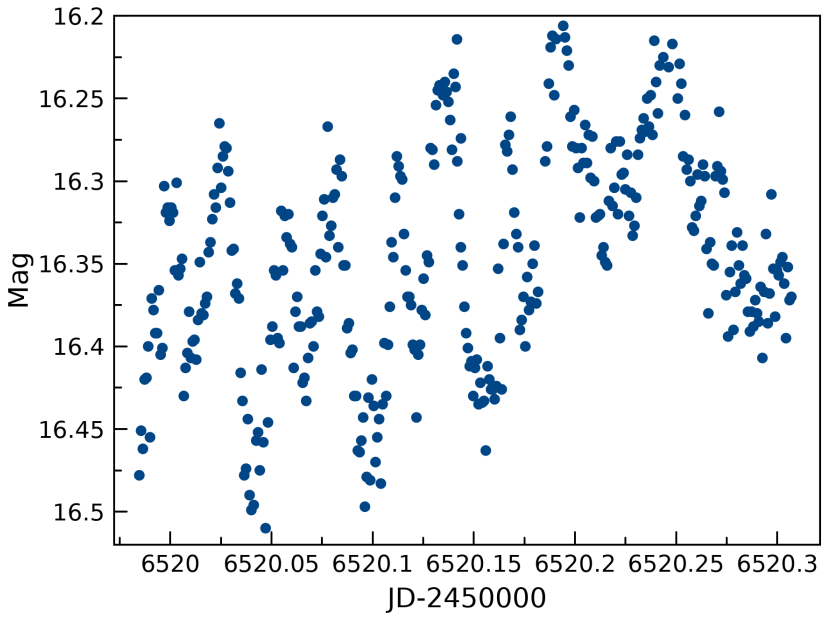

Figure 4: Light curve of BW Scl in quiescence, covering multiple orbital periods ($P_{orb} = 0.054$ d). Data from AAVSO (2019).

5.2 Spectroscopy in Quiescence

In quiescence DN spectra are characterized by strong Balmer lines, which are often double peaked. The double peaks are formed in the accretion disc and the source for its shape is explained in Figure 5. Effect of inclination on the double peaks can be seen in Figure 6, which explains why some objects don't have double peaked emission. Emission lines of He I and a few heavier elements can also be seen. These emission lines are on a continuum, which structure is explained in Figure 7. In objects with low mass-transfer rate white dwarf's broad absorption lines can be seen around Balmer emission. In IR few lines originated from the disc are present. In systems with longer orbital periods spectrum from the secondary dominates, producing spectra typical to K or M class stars.

During the orbital motion, depending on the inclination of the object, parts of the system may be eclipsing. Even if the stars themselves are not eclipsing, parts of the accretion disc may still be eclipsing. This causes the peaks of the double peaked emission lines vary in amplitude. Additionally, the change in the radial velocity of the bright spot over the orbital period causes the bright spot to appear in different parts of the emission line profile. Example of this is presented in Figure 8.

In summary, the spectra consist of contributions from the primary, the secondary, the bright spot and the disc. The relative strengths of these contributions are determined by the orbital period, the mass-transfer rate and the mass ratio(Warner 1995; Hellier 2001). A spectrum of BW Scl, which is representative of typical DN spectrum is in Figure 9.

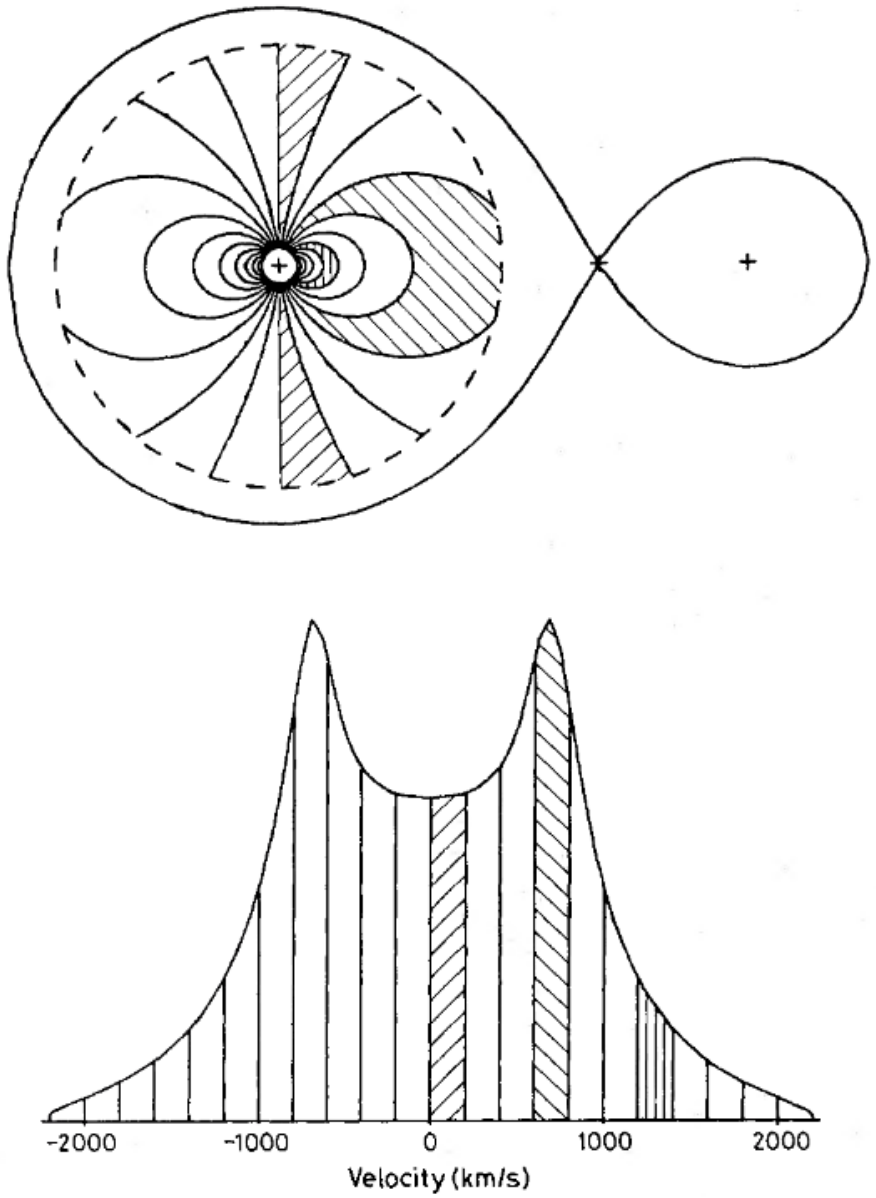

Figure 5: How emission line profile forms in the disc. Areas in the Figure represent equal radial velocity in the observers direction. Shaded regions in the profile originate in the corresponding shaded areas on the disc. From Horne & Marsh (1986).

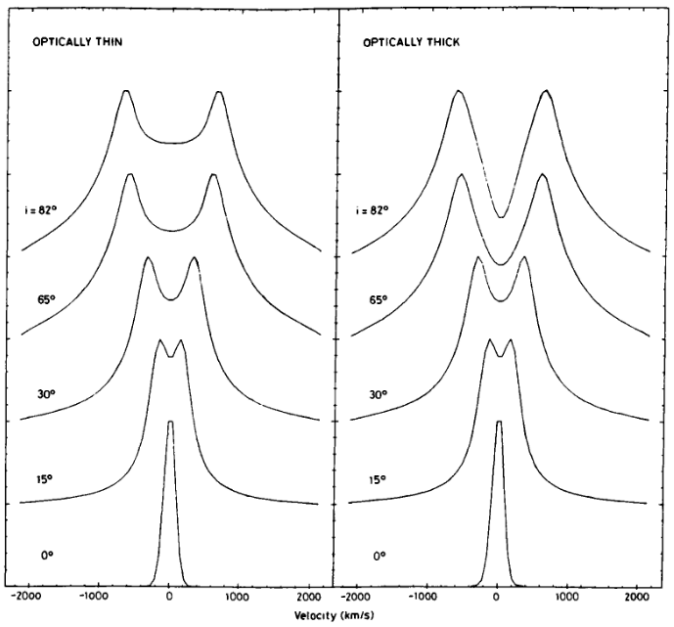

Figure 6: How a disc inclination affects the emission line profile. From Horne & Marsh (1986).

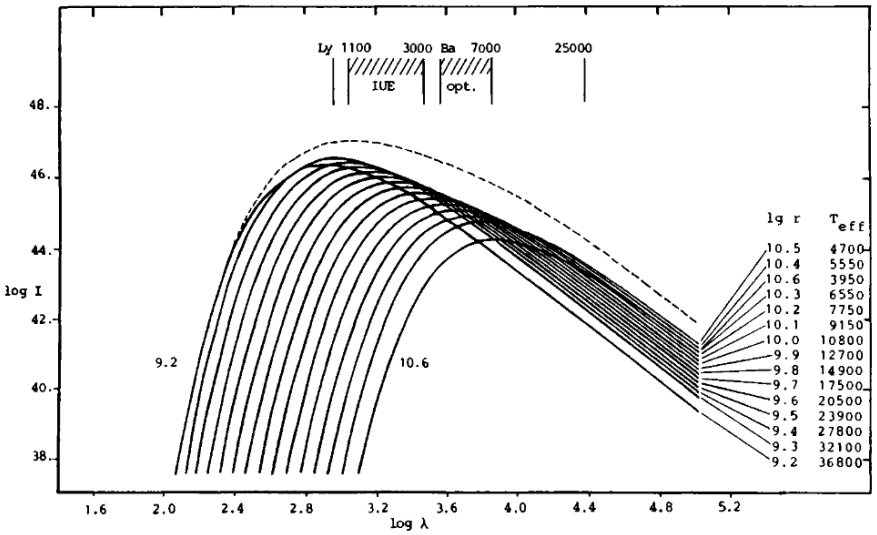

Figure 7: Contributions from individual black body annuli in stationary disc model to the total intensity. Each annuli follows temperature profile discussed in section 4.3. From La Dous (1989).

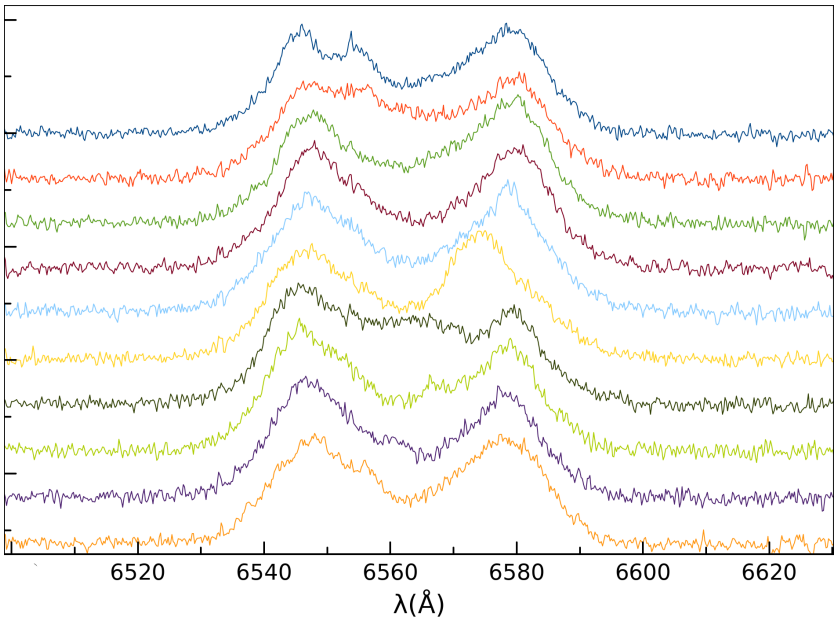

Figure 8: Waterfall image of the phase averaged spectra for the Hα line from X-shooter data. The spectra were binned to 20 phase bins and averaged. For clarity only every other bin is plotted.

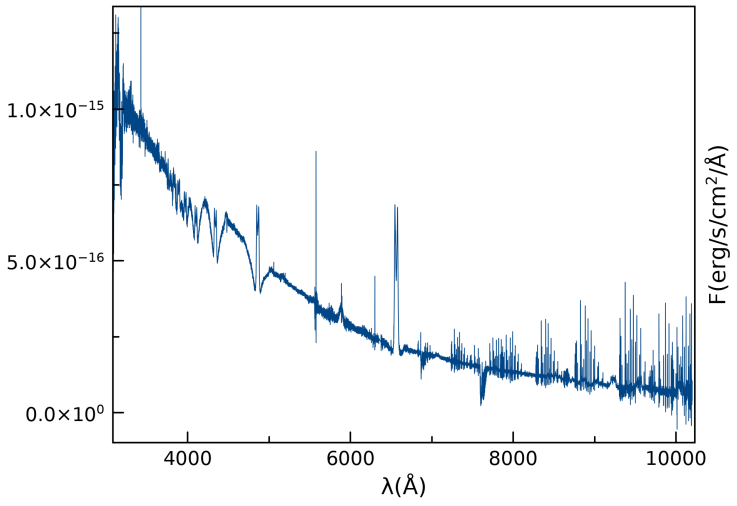

Figure 9: All 239 spectra from X-shooter for BW Scl combined to the single spectrum.

5.3 Photometry in Outburst

The beginning of an outburst is characterized by a rapid increase in brightness, which after reaching maximum brightness decays on much slower timescale. Example of this is in Figure 10. Outbursts can be categorized by different features, most importantly they can be categorized into normal outbursts and superoutbursts. Superoutbursts compared to normal outbursts are brighter by approximately 0.7 mag and last ∼5 times longer. (Warner 1995; Hellier 2001)

In addition, superoutbursts exhibit so-called superhumps. This is a periodic wave in the light curve, superpositioned on the orbital variation. Its period is usually few percent longer than the orbital period and changes during the superoutburst. Source of the superhumps is understood as 3:1 resonance in the disc that produces eccentricity. The difference in the superhump period and the orbital period can be used to estimate the mass ratio of the object (Patterson et al. 2005). Example of the superhumps can be seen in Figure 11.

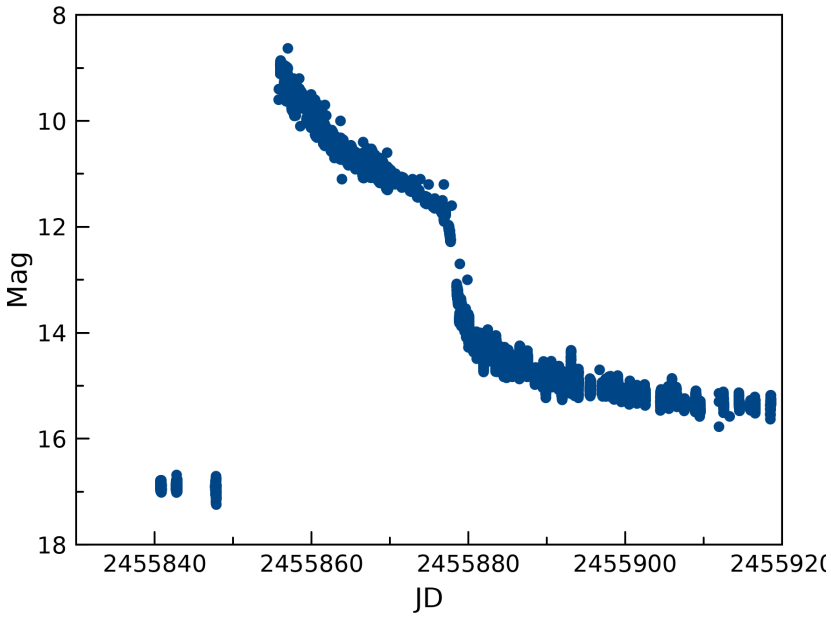

Figure 10: Light curve of BW Scl during its only recorded outburst in 2011. Data from AAVSO (2019).

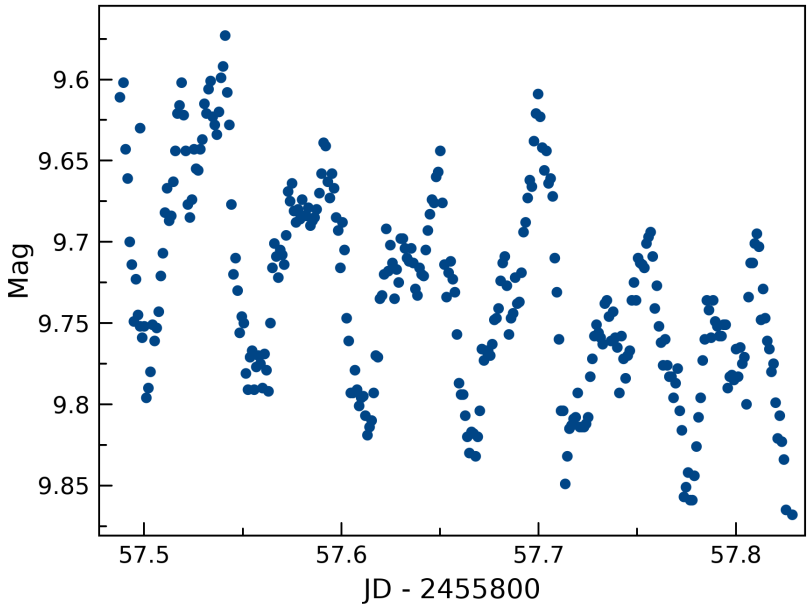

Figure 11: Superhumps in BW Scl during its superoutburst. Data from AAVSO (2019).

5.4 Spectroscopy in Outburst

During the transition from quiescence to outburst the increasing continuum overwhelms the emission-line profile, and broad absorption lines replace the emission-lines. The rise to outburst can be classified to two different types, types A and B. Type A reaches the maximum faster, and starts at longer wavelengths, with delayed rise at shorter wavelengths. Delay from optical to 1000Å is 5-15 h. Type B reaches the maximum slower, and rises almost equally at all wavelengths. Both types decline similarly, starting at all wavelengths simultaneously with UV reaching the minimum first (Warner 1995; Hellier 2001).

6 Disc Instability Model

6.1 Theory

The disc instability model is the currently favored model explaining the mechanics behind DN outbursts. In short, during quiescence material is stored in the disc. Then an instability triggers the stored material's rapid accretion on the primary. This model was proposed by Osaki (1974), Hōshi (1979) and Bath & Pringle (1982).

Material from the secondary is arriving at the disc at rate $\dot{M}_{in}$, and is transferring through the disc at rate $\dot{M}_{tr}$. These rates are not necessarily equal, since $\dot{M}_{in}$ is determined by evolutionary effects of the system, and $\dot{M}_{tr}$ is determined by how efficiently the material is able to shed its angular momentum. This is quantified in variable α, known as disc viscosity parameter.

Solving thermal equilibria for an annulus of the accretion disc involves equating viscous heating and radiative cooling at the surface of the annulus. Heat from the inner and densest parts of the disc needs to be transported to the surface where it can be radiated away. Resulting thermal equilibria in terms of surface density Σ and surface temperature T_{eff} are plotted in Figure 12. The curve can be divided to three distinct regimes. A convective, a radiative and a combination of those two. Convective solution corresponds to a low mass-transfer rate through the annulus, resulting in low temperature, atomic hydrogen, high mass and thus high density, requiring convection for heat transfer. Radiative solution corresponds to high mass-transfer rate and accordingly higher temperature, ionized hydrogen, lower mass and lower density, allowing radiative transfer. Third solution, both convective and radiative, corresponds to the part of the curve where $dT_{eff}/d\Sigma < 0$, separating the other two regimes. In this temperature range, hydrogen is partially ionized, and H^- ions are important source of opacity. Thus the opacity and resulting fraction of flux carried by convection is highly sensitive to temperature, resulting in unstable conditions. Thus, even if a certain mass-transfer rate annulus could find thermal equilibrium in this region, a small perturbation would force it to either of the other two regimes.

Figure 13 displays a simplified S-curve, where Σ_{min} corresponds to $\dot{M}_{crit2}$ and Σ_{max} corresponds to $\dot{M}_{crit1}$. If mass-transfer rate incoming to the annulus $\dot{M}_{in}$ is less than $\dot{M}_{crit1}$, then the annulus can find a stable thermal equilibrium at the lower (convective) branch. Similarly if $\dot{M}_{in}$ is larger than $\dot{M}_{crit2}$, then the annulus can find a stable thermal equilibrium at the upper (radiative) branch. For $\dot{M}_{crit1} < \dot{M}_{in} < \dot{M}_{crit2}$, thermal equilibrium lays on the unstable middle branch, which the annulus cannot occupy. Let's suppose the annulus ends up on the lower branch. Since $\dot{M}_{crit1} < \dot{M}_{in}$, mass will accumulate in

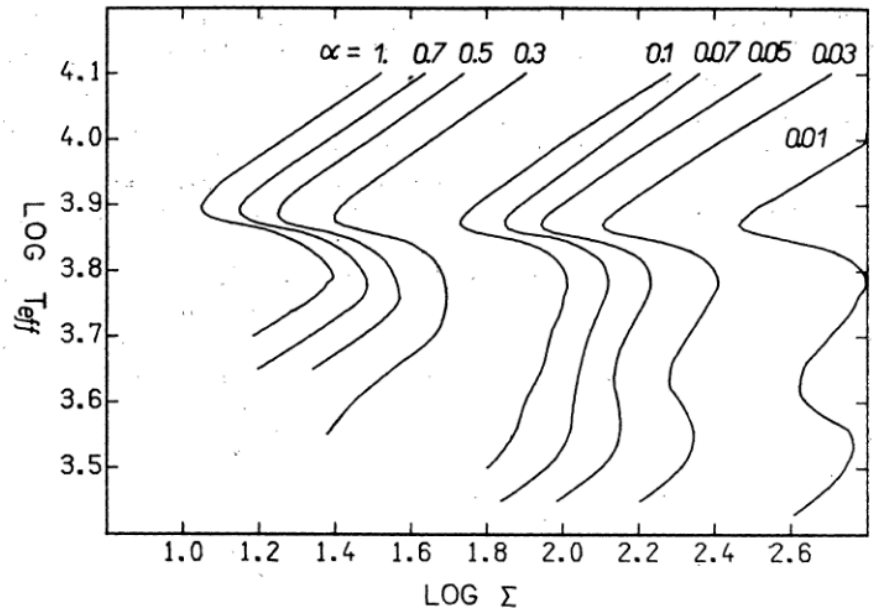

Figure 12: The 'S-curve', relationship between surface density and surface temperature for multiple values of viscosity parameter. From Pojmanski (1986).

the annulus. Increasing Σ gradually increases mass-transfer rate through the disc and T_{eff} as the annulus moves along the lower branch to the right, until it reaches Σ_{max}. Since the annulus cannot continue to the middle branch, it heats up on thermal time scale along the dotted line, until it reaches thermal equilibrium on the upper (radiative) branch. There the process reverses and the annulus evolves leftwards along the upper branch, as the annulus has $\dot{M}_{in} < \dot{M}_{crit2}$. Once it reaches Σ_{min}, it cannot continue to the middle branch, instead it cools down on thermal time scale, restarting the cycle. Therefore the annulus cycles between upper and lower states, in a limit cycle.

In a whole disc each individual annuli interacts with neighboring annuli and exchanges heat and material with them. If an annulus in any part of the disc transitions in higher state, it has an increased T_{eff} and Σ, and thus transfers heat and material to its neighboring annuli at an increased rate. This triggers transition to the higher state in the neighboring annuli, producing a heating wave propagating through the disc. Later on the first annulus to cool to the lower state produces a propagating cooling wave.

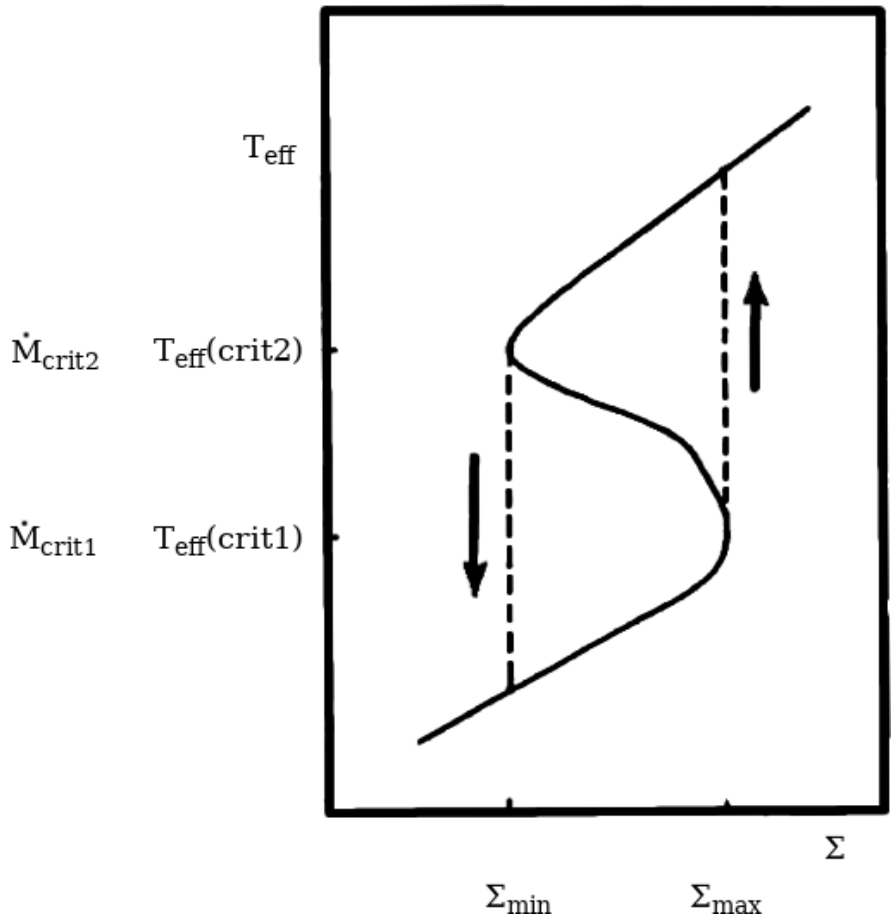

Figure 13: Schematic 'S-curve', illustrating the thermal limit cycle. From Warner (1995).

6.2 Effect on Outburst Morphology

Location of the first annulus determines whether the heating/cooling wave is propagating inwards or outwards. Outburst that starts in the outer parts of the accretion disc moves faster than one starting in the inner parts. This is because in the former case, low viscosity regions are surrounded by higher viscosity regions. This enables the heating wave to propagate faster as the annuli in transition are able to efficiently transport angular momentum outwards. On the contrary the outwards propagating heating wave is surrounded by lower viscosity regions, making angular momentum transfer outwards slower. Thus inwards propagating wave transitions the disc from quiescence to outburst faster than outwards propagating one, producing steeper light

curves. This explains the difference between type A(fast) and B(slow) outbursts (Warner 1995).

Outburst doesn't necessary return the disc to its original state. In model proposed by Ichikawa et al. (1993) for systems with low mass ratio q < 0.22 subsequent outbursts leave the accretion disc with increasing amount of mass and angular momentum. Eventually the disc becomes large enough that the outer edge reaches radius at which it is in 3:1 resonance with the secondary. Tidal dissipation at the disc edge maintains it at high viscosity state, prolonging the outburst to a superoutburst, thus allowing the accumulated mass to be accreted on the primary, and the angular momentum to be dissipated.

7 CV Evolution

7.1 Stability of Mass-Transfer

The total angular momentum J of the system is

$$J = (M_1 a_1^2 + M_2 a_2^2)\Omega \tag{5}$$

where M_1 and M_2 are the masses of the primary and the secondary respectively, a_1 and a_2 are the distances to the center of mass and Ω is the angular velocity. Substituting $a_1 = \frac{M_2}{M}a$, $a_2 = \frac{M_2}{M}a$ and

$$\Omega = \sqrt{\frac{G(M_1 + M_2)}{a^3}} \tag{6}$$

we get

$$J = M_1 M_2 \sqrt{\frac{Ga}{M}} \tag{7}$$

Differentiating this with respect to time and assuming conservative mass transfer, $\dot{M} = 0$ and $\dot{M}_1 = -\dot{M}_2$, we get

$$\dot{J} = \dot{M}_1 M_2 \sqrt{\frac{Ga}{M}} + \dot{M}_2 M_1 \sqrt{\frac{Ga}{M}} + \frac{1}{2} M_1 M_2 \frac{G}{M} \left(\frac{Ga}{M}\right)^{-1/2} \dot{a} \tag{8}$$

Assuming that the total angular momentum conserves $\dot{J} = 0$, and dividing by J, we get

$$\frac{\dot{a}}{a} = -2\frac{\dot{M}_2}{M_2}\left(1 - \frac{M_2}{M_1}\right) = -2\frac{\dot{M}_2}{M_2}(1 - q) \tag{9}$$

Thus, if q > 1, mass-transfer results in stars getting closer. This leads to more mass-transfer and a runaway process. If q < 1, mass-transfer results in stars getting further apart, shutting off the mass-transfer.

To complicate things, mass-transfer leads to a diminishing mass-ratio, resulting in a change in Roche-lobe geometry. Approximation for the size of the secondary's Roche-lobe by Paczyński (1971) is

$$\frac{R_L}{a} = 0.462 \left(\frac{q}{1+q}\right)^{1/3} \tag{10}$$

Differentiating this gives

$$\dot{R_L} = 0.462 \frac{1}{3} \left(\frac{q}{1+q}\right)^{-2/3} \left(\frac{\dot{q}}{1+q} - \frac{\dot{q}q}{(1+q)^2}\right) a + 0.462 \left(\frac{q}{1+q}\right)^{1/3} \dot{a} \tag{11}$$

Substituting in time derivative of mass ratio q

$$\dot{q} = \frac{\dot{M_2}}{M_2} q(1+q) \tag{12}$$

gives

$$\dot{R_L} = 0.462 \frac{1}{3} \frac{\dot{M_2}}{M_2} \left(\frac{q}{1+q}\right)^{1/3} a + 0.462 \left(\frac{q}{1+q}\right)^{1/3} \dot{a} \tag{13}$$

Dividing by R_L and substituting in $\frac{\dot{a}}{a}$ gives

$$\frac{\dot{R_L}}{R_L} = \frac{2\dot{M_2}}{M_2} \left(q - \frac{5}{6}\right) \tag{14}$$

Thus, q < $\frac{5}{6}$ produces stable, self-regulating mass-transfer.

7.2 Response to the Mass Loss

The secondary responds to the mass loss on two time scales, dynamical and thermal. Dynamical time scale is the characteristic sound-crossing time of the region, and is given in the equation 15, where $\overline{\rho}(r)$ is the mean density within r.

$$\tau_{dyn} = \frac{1}{\sqrt{G\overline{\rho}(r)}} \tag{15}$$

Thermal time scale is determined by the rate at which heat can diffuse in the star, and is given by the equation 16, where n is the polytropic index

of the secondary, and M_2, R_2, L_2 are the mass, radius and luminosity of the secondary respectively.

$$\tau_{th} = \frac{3}{10 - 2n} \frac{GM_2^2}{R_2 L_2} \tag{16}$$

Dynamical time scale is in order of hours, and thermal time scale is in order of millions of years. Thus it is safe to assume that secondaries in mass-transferring systems are in dynamic equilibrium, but out of thermal equilibrium. Since main sequence stars with lower mass are smaller in radius and have lower surface temperature, secondaries in mass-transferring systems are larger and hotter than in isolation, and are trying to re-establish this condition.

7.3 Angular Momentum Loss

A system with q $< \frac{5}{6}$ reacts to mass-transfer by increasing the distance between the stars. Thus continued stable mass-transfer requires a mechanism to counteract the increasing separation through angular momentum loss. These mechanisms are magnetic braking and gravitational radiation.

7.3.1 Magnetic Braking

Magnetic braking is caused by the coupling of a star's magnetic field to the ionized stellar wind. As a star rotates, it drags the expanding wind along the magnetic field lines. The angular momentum loss rate by Kawaler (1988) is

$$\dot{J} = \frac{2}{3} \dot{M} R^2 \Omega \left[\frac{r_A}{R} \right]^n \tag{17}$$

where $\dot{M}$ is mass-loss rate due to stellar wind, R is stellar radius, Ω is angular velocity, r_A is Alfvén radius, and n is 1 for radial field geometry, or 2 for dipole. Main concerns on the magnetic braking efficiency are $\dot{M}$ and r_A/R, since they vary greatly between models and spectral classes of stars. Secondaries in CVs can be assumed to be tidally locked, and thus Ω is simply the orbital period P_{orb}. Magnetic braking drains angular momentum from the secondary, which is coupled to the angular momentum. Loss in orbital angular momentum leads to reduced separation and shorter P_{orb}, which paradoxically results in more rapid rotation of the secondary.

7.3.2 Gravitational Radiation

General Relativity states that a binary will lose angular momentum at rate described by Landau et al. (1952) in equation 18

$$\frac{\dot{J}}{J} = -\frac{32G^3}{5c^3}\frac{M_1 M_2 (M_1 + M_2)}{a^4} \tag{18}$$

a^{-4} dependence implies rapid increase at smaller separations, but this is somewhat counteracted by lower M_2 in systems with small a.

7.4 Period Gap

Plotting periods of known CVs as is done in Figure 14, reveals a clear pattern. There exists a clear minimum period $\sim$ 75min, and drastically lower population with orbital periods between $\sim$ 2 and $\sim$ 3 hours, called period gap.

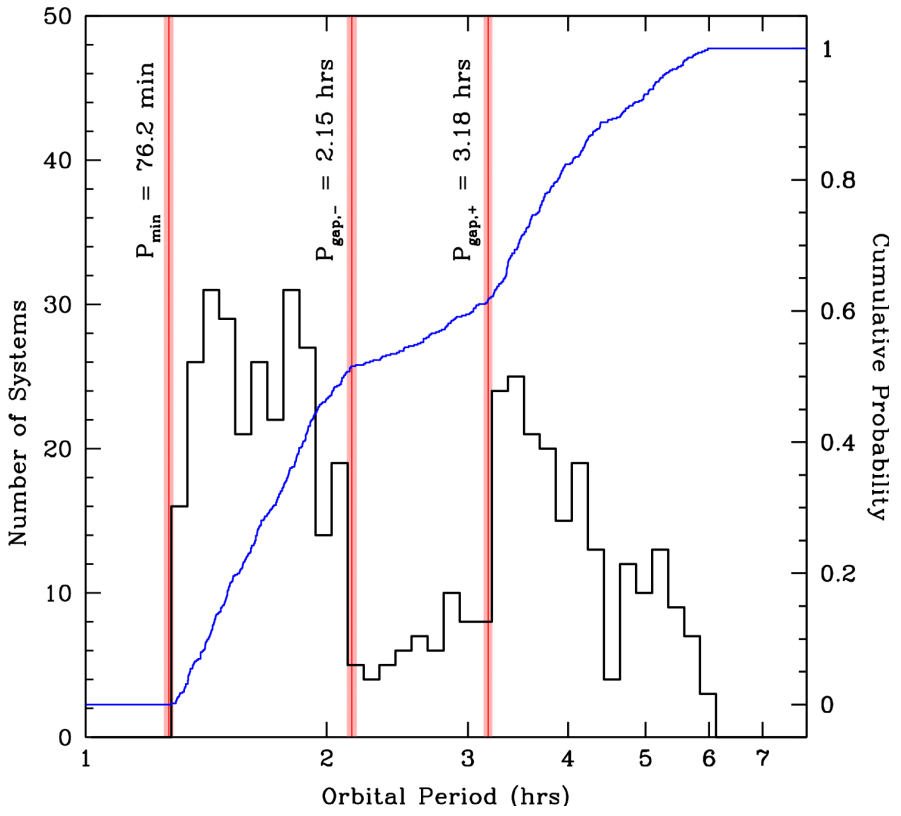

Figure 14: Orbital periods of CVs plotted against number of systems in this period bin. Red vertical lines indicate the minimum period and the period gap. Blue line indicates the cumulative population. From Knigge (2006).

The upper edge of the period gap corresponds roughly to a mass range of secondaries where the internal structure changes. Above the upper edge

the secondaries have radiative cores, and below they are thoroughly convective. This change in the inner structure weakens the magnetic field of the secondary, effectively turning off magnetic braking. Weakened angular momentum loss results in lowered mass-transfer rate, allowing the secondary to establish thermal equilibrium, shrinking in size. The secondary detaches from its Roche-lobe, ceasing mass-transfer altogether. The system then slowly spirals in as a detached binary due to angular momentum loss caused by gravitational radiation and any residual magnetic braking.

Eventually the slow evolution causes the secondary to refill its Roche-lobe, and re-emerge as a CV at the lower edge of the period gap. Since the evolution is solely driven by gravitational radiation, the mass-transfer rate is very low.

7.5 Period-Minimum and Period-Bouncers

CV orbital period distribution drops sharply to zero near $\sim$ 75 min. Secondaries in these systems have masses $\lesssim 0.08\ M_{\odot}$, corresponding to the point where the secondary becomes a sub-stellar brown dwarf. These non-relativistic degenerate objects are well described by a polytrope with polytropic index n=1.5, and their mass-radius relationship is in equation 19, where X is the fractional hydrogen content (Chandrasekhar 1939).

$$R \approx 8.96 \times 10^{8} (1+X)^{5/3} M^{-1/3} \text{ cm} \tag{19}$$

As opposed to main sequence stars, brown dwarfs increase in radius with lower mass. Combining equations 6, 10 and 19 gives

$$P_{orb}(h) \approx 1.41 \times 10^{-2} (1+X)^{5/2} M^{-1} \tag{20}$$

thus transferring mass from the secondary increases the orbital period. This can be qualitatively justified the following way. Mass-transfer increases the orbital separation because q $<$ 1. This increase is counteracted by angular momentum loss mechanism. If the secondary shrinks in size, the centers of mass of the respective stars need to be closer together in order to keep the secondary in contact with its Roche-lobe. Respectively if the secondary increases in size, the centers of mass don't need to come as close together as before in order to keep the secondary in contact with the Roche-lobe.

These systems with brown dwarf secondaries and increasing orbital period are known as "period-bouncers". Standard model of CV evolution predicts that 40-60% of the CVs should be post-period-minimum systems (Goliasch & Nelson 2015), but only a handful of these are known(Kimura et al. 2018; Patterson et al. 2005). The absence of predicted amount of period-bouncers

has been a source of frustration for the past decades and casts doubts on our understanding of compact binary evolution in general. Therefore the primary aim of this thesis is to determine the evolutionary status of BW Scl.

8 BW Sculptoris

BW Scl was initially found as a bright X-ray source in ROSAT catalogue in 1990 (Abbott et al. 1997) and independently as a brigth UV source in Hamburg/ESO survey (Augusteijn & Wisotzki 1997). Its optical counterpart was found in 1992, and was recognised as a CV (Abbott et al. 1997). Measurement of orbital parameters by Augusteijn & Wisotzki (1997) in 1995 with EFOSC2 (ESO/NTT) found $P_{orb} \approx 78$ min, which was the lowest known at the time. The same study also found radial velocity semi-amplitude $K = 55 \pm 5$ km/s and systemic velocity $\gamma = 1 \pm 3$ km/s. In 2002 Mennickent et al. (2004) observed BW Scl in IR with ISAAC (ESO/VLT), but didn't find any sign of the secondary. Observations in 1999 with the Hubble space telescope by Gänsicke et al. (2005) found the white dwarf effective temperature to be $T_{eff} = 14800 \pm 900$ K.

On October 21st 2011, BW Scl was observed at 9 mag (AAVSO 2019), when its usual quiescent brightness is around $16 < m_V < 17$ mag. (Augusteijn & Wisotzki 1997; Uthas et al. 2012; AAVSO 2019). This was its first and only observed outburst, peaking at $m_V = 8.9$ mag (AAVSO 2019). BW Scl was observed by variety of telescopes from 1999 to 2009 by Uthas et al. (2012). Their analysis resulted in accurate measurement of the orbital period $P_{orb} = 78.22639 \pm 0.00003$ min. $= 0.05432392 \pm 0.00000002$ d. They also found signs of quiescent superhumps with period $P_{sh} = 87.27$ min. From the 2011 superoutburst Kato et al. (2013) measured a superhump period $P_{sh} = 78.984 \pm 0.011$ min $= 0.05500 \pm 0.000008$ d, and came to a classification of WZ Sge for BW Scl due to the outburst morphology. Finally recent parallax measurements by Gaia found the distance to be $d = 94.4 \pm 0.9$ pc (Gaia Collaboration et al. 2016, 2018).

9 Observations

We use data from multiple instruments, telescopes and amateur astronomers. The spectra were obtained in 2001, 2002, 2010 and 2018 using the EFOSC2 (ESO NTT), the X-shooter (ESO VLT) and the UVES (ESO VLT) instruments. BW Scl was also observed by AAVSO amateur astronomers from late 2001 onwards. Figure 15 shows the dates of the observations with the light curve of BW Scl.

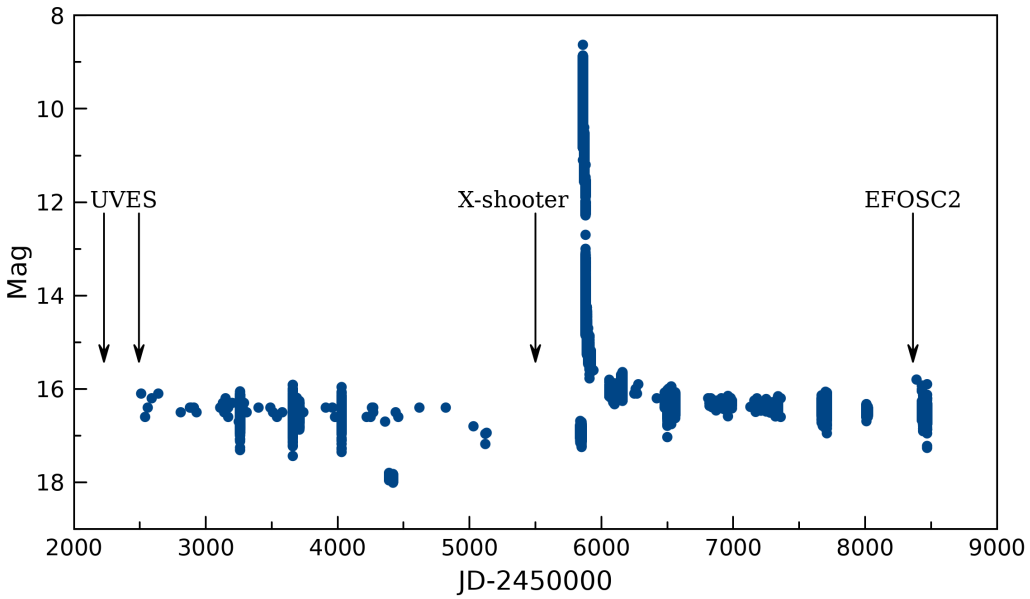

Figure 15: Times of the three observations marked on the light curve. Light curve contains all observations in all filters, excluding measurements with only upper limit for the brightness. Data from AAVSO (2019).

9.1 EFOSC2

ESO Faint Object Spectrograph and Camera (EFOSC2) is mounted at the ESO NTT. EFOSC2 is a focal reducer multi-mode instrument, covering wavelength range from 3050 Å to 11000 Å.

BW Scl was observed on September 24th 2018. Data consists of 22 spectra taken with grism 18, one spectrum with grism 4 and one spectrum with grism 7. Grism 18 measurements covered 1 orbital period. Wavelength ranges and resolutions for the grisms: 4700 Å - 6770 Å with the resolving power R$\sim$1000

for grism 18, 4085 Å - 7520 Å with R∼600 for grism 4 and 3270 Å - 5240 Å with R∼750 for grism 7. Exposure times for grism 18 were 180 s whereas for both grism 4 and grism 7 300 s was used (Buzzoni et al. 1984).

Based on data products from observations made with ESO Telescopes at the La Silla Paranal Observatory under programme ID 0101.D-0806(B).

9.2 X-shooter

X-shooter is a second generation instrument at the ESO VLT. It is a single target, intermediate resolution spectrograph and it covers wavelengths from 3000 Å to 25000 Å. The incoming light from the telescope is split to three échelle spectrographs optimized for UV-Blue (UVB), Visible (VIS) and Near-IR (NIR) wavelengths (Vernet et al. 2011).

BW Scl was observed on October 11-13th 2010. The data consists of 239 spectra in UVB and VIS with 60 s exposure times, no useful NIR data was obtained. The resolving power for the UVB arm was 8900 and for the VIS arm it was 5400. The observations covered ∼4.2 orbital periods.

Based on data products from observations made with ESO Telescopes at the La Silla Paranal Observatory under programme 086.D-0775(A).

9.3 UVES

UVES is an instrument at the ESO VLT. UVES is a cross-dispersed échelle spectrograph operating from 3000 Å to 11000 Å. The incoming light is split in two arms (UV to Blue, and Visual to Red) within the instrument (Dekker et al. 2000).

BW Scl was observed on November 13-15th 2001 and on August 8-9th 2002. The data consists of 60 blue-arm spectra from 13-14 November 2001 covering ∼4.2 orbital periods, 15 dichroic 1 (both arms) spectra from 15 November 2001 covering 1 orbital period, 30 blue-arm spectra from 15 November 2001 covering ∼3.2 orbital periods, and 41 blue-arm spectra from 8-9 August 2002 covering ∼2.4 orbital periods. All of the UVES observations had 300 s exposure times. Resolving power for both arms was ∼44000.

Based on data products from observations made with ESO Telescopes at the La Silla Paranal Observatory under programme 68.D-0153(A) and 69.D-0391(A).

10 Data Reduction

10.1 EFOSC2

Data reduction for the EFOSC2 data was performed using Image Reduction and Analysis Facility (`IRAF`) created by National Optical Astronomy Observatory (NOAO)(Tody 1986). The reduction steps were the followings: bias, flats, wavelength calibration and flux calibration. Dark reduction was deemed unnecessary due to the instrument's negligible dark structure.

10.2 X-shooter and UVES

Data reduction for the X-shooter and the UVES data was done using `EsoReflex` (Freudling et al. 2013). `EsoReflex` is an environment developed to reduce VLT/VLTI science data using the ESO pipelines. Figure 16 shows the GUI for the `EsoReflex`.

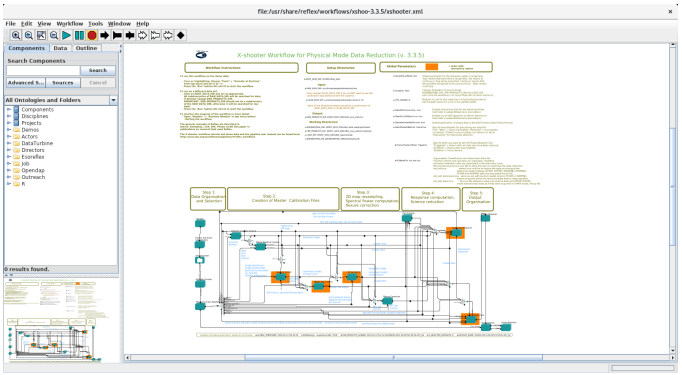

Figure 16: `EsoReflex` in X-shooter workflow.

`EsoReflex` performs all the standard steps to reduce raw scientific data: dark, bias, flats, wavelength calibration and flux calibration to name a few. The user can manually control the steps, or allow the program to work on its own. Resulting reduced data for X-shooter and UVES depends whether the program was run in nodding mode or stare mode. In stare mode each raw image results in 10 reduced files, containing 1-dimensional and 2-dimensional spectra, with and without flux calibration, and sky spectra.

11 Overview of Spectral Features in BW Scl

In this section we will highlight the most important spectral features of BW Scl in the UV and the visual wavelengths. Figures in this section are from X-shooter data, since it has the best signal to noise ratio. All of the 239 individual spectra are averaged together, and both the UV and visual arm spectra are combined together.

Figure 17 shows strong, double peaked hydrogen Balmer-series lines, originating from the accretion disc and the bright spot. These emission lines sit in wide absorption troughs, which originate on the white dwarf. The same figure also shows two helium emission lines. Their shape differs from the Balmer lines, since the accretion disc is not hot enough to excite helium atoms. Instead the emission comes primarily from the bright spot, where the temperature is sufficient.

Figure 18 shows a Mg II absorption at 4481 Å. This line is produced solely on the white dwarf itself, allowing accurate radial velocity measurement, as the white dwarf moves during the orbital period. The absorption line is also gravitationally red-shifted, allowing estimation for the white dwarf's mass and radius.

Figure 19 shows two Ca II emission lines at 8498.02 Å and 8542.09 Å, both of which are situated between telluric O-H lines. The Doppler maps and trailed spectra suggest the source of the Ca II emission lines at IR to be the secondary star.

Figure 20 shows a Ca II emission at 3933.664 Å, located between the Hϵ and Hζ emission lines. The emission is double peaked, but the slanted continuum makes it hard to see. The Doppler maps and trailed spectra suggest the source of it to be the bright spot.

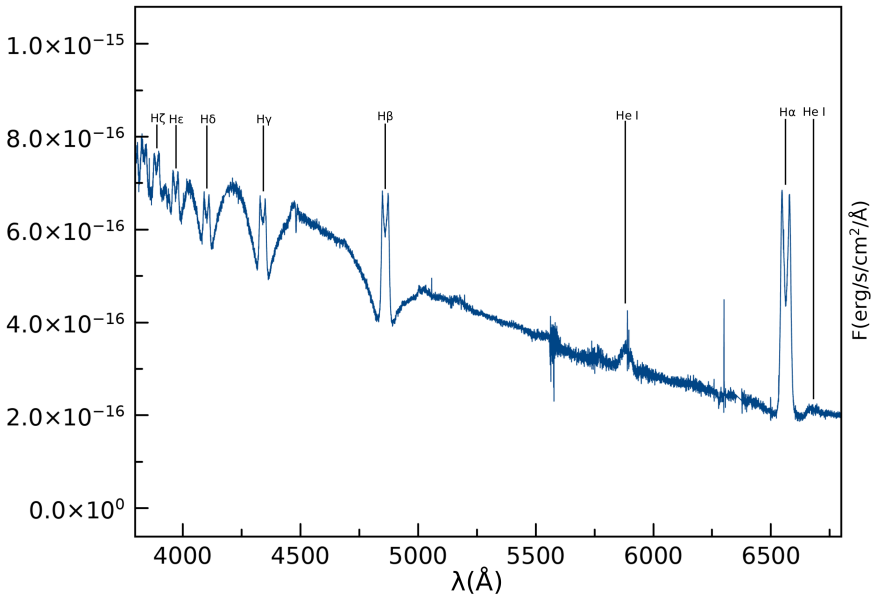

Figure 17: The Balmer series and two helium emission lines.

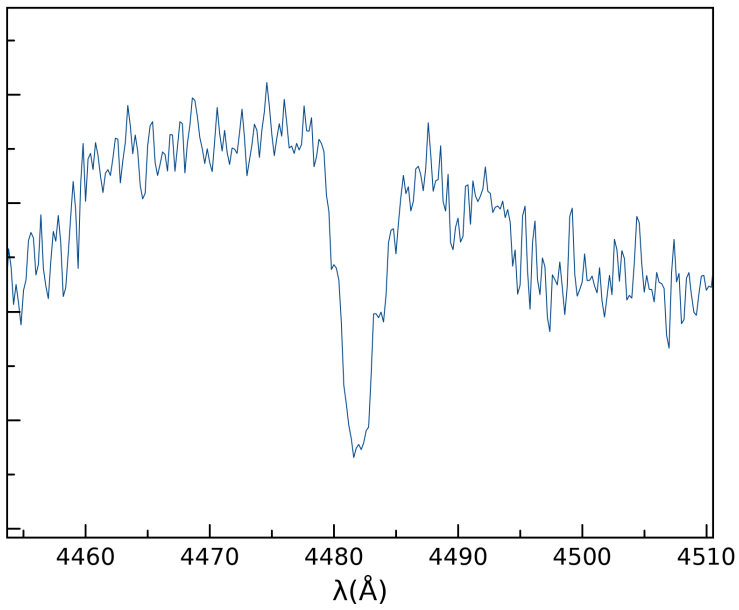

Figure 18: Mg II absorption at 4481 Å, originating from the white dwarf.

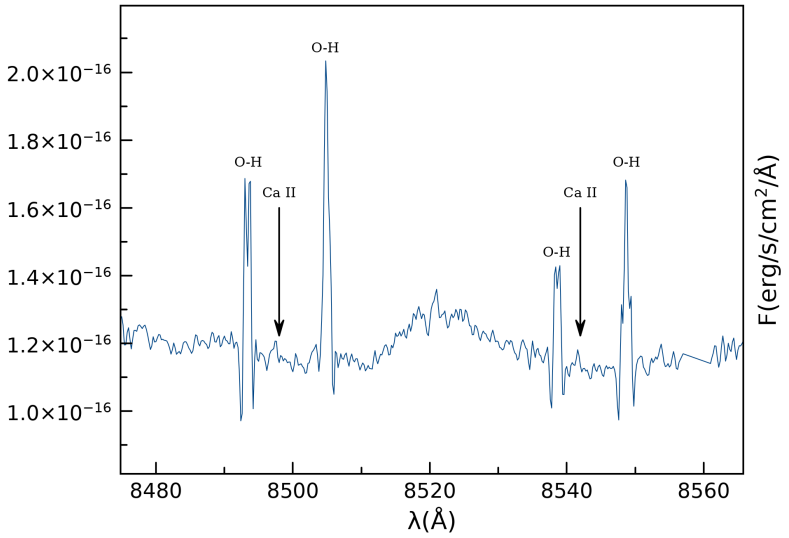

Figure 19: Two Ca II emission lines at 8498.02 Å and 8542.09 Å. Both lines are between two telluric O-H lines.

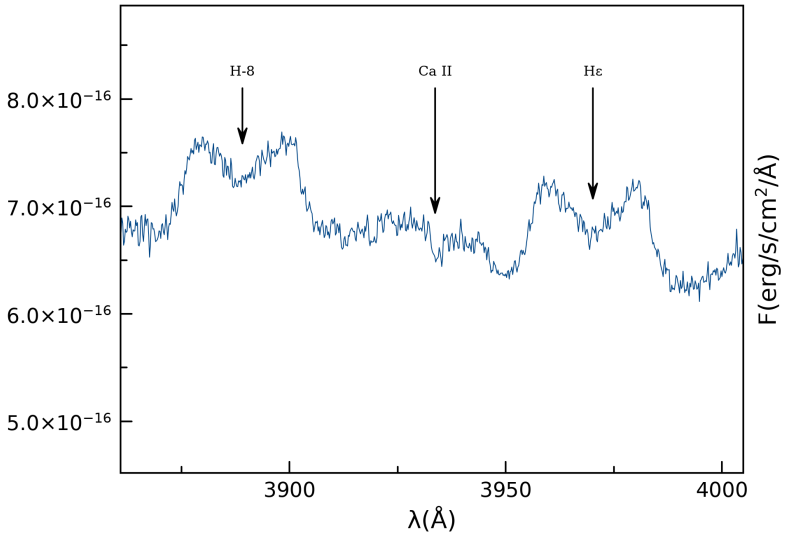

Figure 20: Ca II emission line at 3933.664 Å, located between Hϵ and Hζ.

12 The Radial Velocity Curve

12.1 Double Gaussian Method

Since the primary is difficult to observe directly, radial velocities are often deduced from the emission lines originating from the accretion disc. Outer parts of the disc are more likely to be dominated by tidal and stream interactions, whereas the inner parts of the disc are more likely to be following the orbital motion of the primary. Light from the inner parts of the disc is seen in the wings of the emission line, and is heavily affected by the noise. The method of choice for measuring the velocities of the line wings was so-called double-Gaussian method suggested by Young & Schneider (1980).

Acquiring the wavelength of the extreme wing in spectrum $S(\Lambda)$ requires solving the equation 21, where $K(x)$ is given by equation 22 (Shafter 1983).

$$\int_{-\infty}^{\infty} S(\Lambda)K(\lambda - \Lambda)d\Lambda = 0 \tag{21}$$

$$K(x) = \exp[-(x-\Delta)^2/2\sigma^2] - \exp[-(x+\Delta)^2/2\sigma^2] \tag{22}$$

In practice this means setting up two Gaussian bandpasses at distance Δ from each other (0.5Δ from the line center), and measuring the counts through both of them. The equation 21 is satisfied, when the counts are equal. The resulting line velocities can then be combined with respective orbital phases, and fitted to equation 23, where γ is the spatial velocity of the system, K_1 is the semi-amplitude of the primary, t_0 is the zero phase and P is the period.

$$V(t) = \gamma + K_1 \sin[2\pi(t - t_0)/P] \tag{23}$$

The process of determining γ, K_1 and t_0 starts by selecting σ according to the signal-to-noise ratio of the data and the spectral resolution. Then the Δ is varied, starting well below the wing and ending where the noise starts to dominate. Resulting values for γ, K_1 and t_0 are calculated, with respective errors. The fractional error in K_1, σ_K/K_1, is dependent of Δ, having higher values with low and high values of Δ. This can be understood the following way. Low values of Δ are still tracking outer parts of the disc, which are distorted by tidal effects and the stream. High values of Δ have reached the end of the wing, and are just measuring noise. Thus the optimal value for Δ is after the minimum of σ_K/K, and just before it starts to rapidly rise. This needs to be evaluated further though. For example, evaluating the fractional error in K_1 for EFOSC2 data in Figure 23 suggests two possible values for Δ. One local minimum around $\Delta = 2800$ km/s and another around $\Delta = 3300$

km/s. Transforming these velocities to wavelengths and placing them in the double peak itself as is done in Figure 21 we can determine which of these Δ values is better. $\Delta = 2800$ km/s indicated by red arrow is clearly still within the emission line, but the black arrow indicating $\Delta = 3300$ km/s starts to be on the noise dominated regime. Thus $\Delta = 2800$ km/s is chosen for EFOSC2 data.

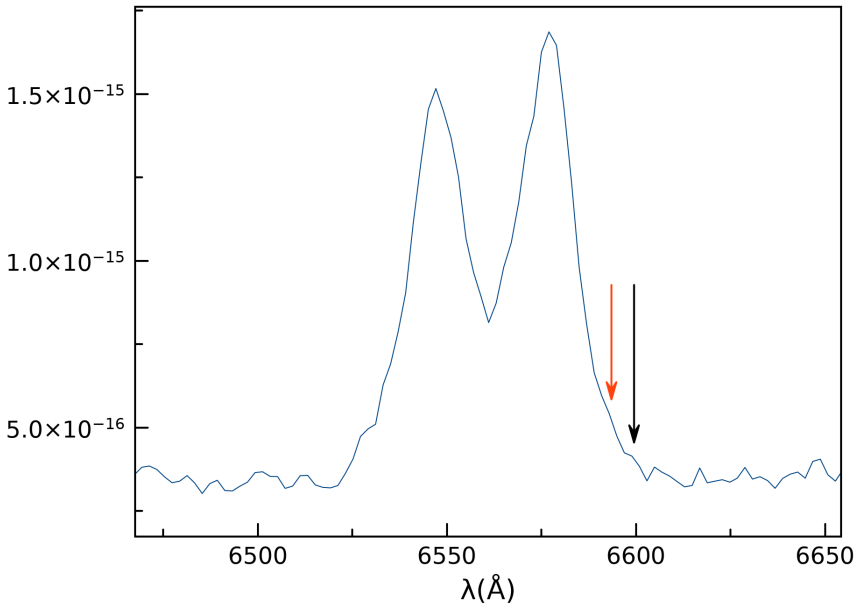

Figure 21: Hα line from EFOSC2 data. Red arrow indicates $\Delta = 2800$ km/s and black arrow indicates $\Delta = 3300$ km/s.

In Figures 22-24 are values of γ, K_1 and ϕ, where the ϕ is the zero phase for that dataset. Time of the inferior conjunction is chosen as the t_0. Values of γ, K_1 and ϕ are stable before and until the end of the wing determined from the σ_K. Similarly their error stays stable until the end of the wing.

12.2 Results

To reduce noise the X-shooter spectra were averaged to 20 phase bins equally spaced around the orbit. Number of individual spectra in each bin varies between 9 and 15, averaging at 12 spectra per bin. EFOSC2 or UVES spectra were not averaged, as this would have eroded the time-resolution too much. The results are collected in table 1 for each dataset. The EFOSC2 data was deemed too noisy, and thus excluded from further analysis. The averages between the X-shooter and the UVES datasets are comparable to the results by Augusteijn & Wisotzki (1997) considering the uncertainties.

Table 1: Values for parameters determined by the double Gaussian method.

Data source	Δ(km(s)	K_1(km/s)	γ(km/s)	ϕ
X-shooter	2500	39.7±3.2	-9.6±2.2	0.17±0.01
EFOSC2	2800	71.9±14.3	6.5±10.1	0.01±0.03
UVES	2800	45.4±7.5	23.1±5.4	0.12±0.03

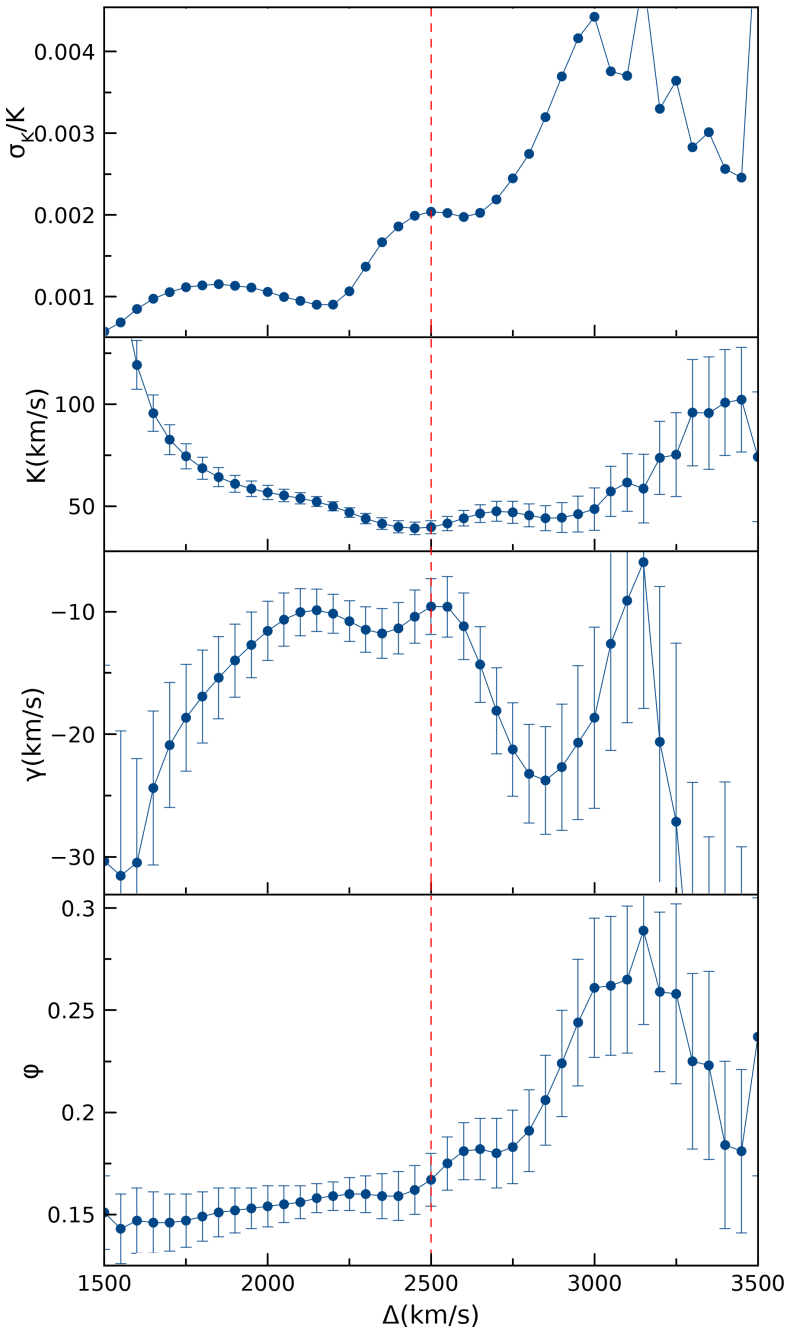

Figure 22: Results from the double Gaussian method for the X-shooter data. From top to bottom: Fractional error in WDs radial velocity K_1, K_1, systemic velocity γ and zero phase ϕ. Red dashed line indicates the best value for Δ.

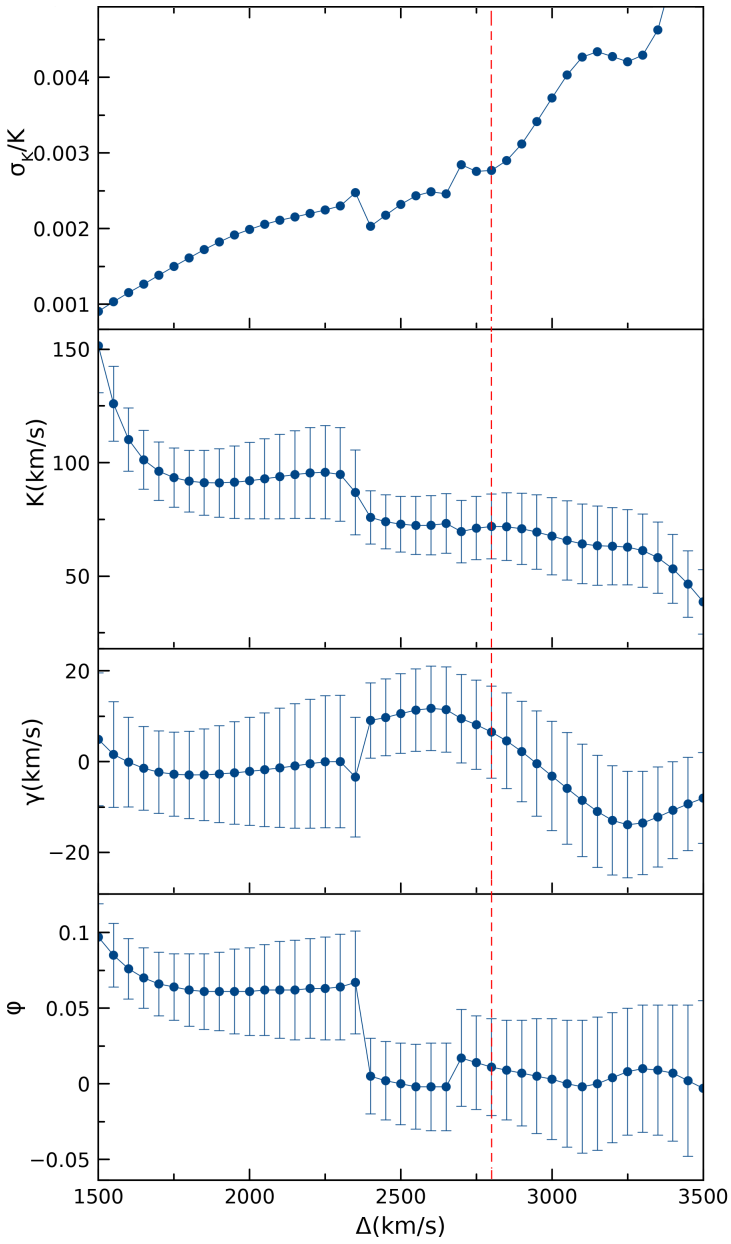

Figure 23: Results from the double Gaussian method for the EFOSC2 data. From top to bottom: Fractional error in WDs radial velocity K_1, K_1, systemic velocity γ and zero phase ϕ. Red dashed line indicates the best value for Δ.

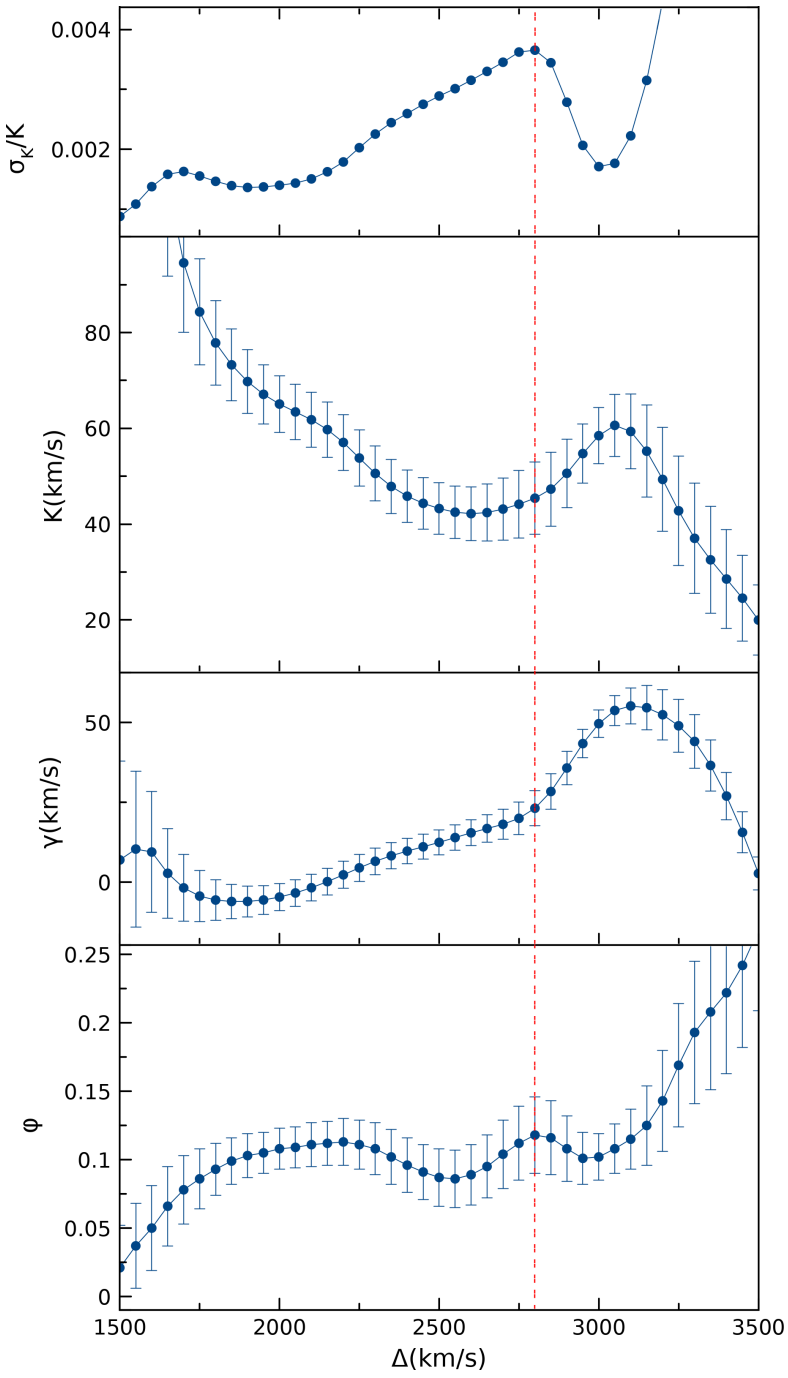

Figure 24: Results from the double Gaussian method for the UVES data. From top to bottom: Fractional error in WDs radial velocity K_1, K_1, systemic velocity γ and zero phase ϕ. Red dashed line indicates the best value for Δ.

13 Determination of Orbital Parameters

13.1 Mg II line absorption

In some white dwarfs the Mg II absorption line at 4481 Å is visible, this is the case for BW Scl. Since this absorption is originated on the white dwarf itself, it follows the motion of it better than inner parts of the accretion disc. The absorption line is shown in Figure 18.

The X-shooter data was binned to 20 bins equally spaced by orbital phase. Then the absorption profiles were fitted with single Gaussian absorption profile with `IRAF`. For some phases this wasn't possible, since the nearby He I line at 4471 Å originating from the disc was overlapping with the absorption line. Resulting line velocities were then fitted with a sine function. Resulting radial velocity was $K_1 = 43 \pm 7$ km/s and the system velocity $\gamma = 59.6 \pm 5.4$ km/s.

13.2 White Dwarf Mass

The discrepancy in system velocities between ones obtained from the accretion disc (Hα) and the white dwarf itself (Mg II) is caused by gravitational redshift. This can be used to measure the mass of the white dwarf, as done by Pala et al. (2019), originally described by Greenstein & Trimble (1967). Since gravitational redshift depends on the surface gravity of the white dwarf, it is dependent on the mass-radius relation of the white dwarf. This is described in equation 24, where γ_{WD} and γ_{sec} are spatial velocities determined for white dwarf and the whole system respectively.

$$V_{grav}(\mathrm{WD}) = \gamma_{WD} - \gamma_{sec} = 0.635 \frac{M_{WD}}{M_\odot} \frac{R_\odot}{R_{WD}} \mathrm{km/s} \tag{24}$$

For the mass-radius relation, a zero temperature carbon white dwarf model by Hamada & Salpeter (1961) was used, and $\gamma_{sec} = 1 \pm 3$ km/s by Mennickent et al. (2004). Results were: $M_{\mathrm{WD}} = 0.84 \pm 0.04\ M_\odot$ and $R_{\mathrm{WD}} = 0.011 \pm 0.002\ R_\odot$.

13.3 Mass-ratio and Secondary Mass

Assuming that the system rotates on circular orbit, edge-on viewing and by combining the definition for the center of mass and equation 6 we get:

$$K_1 = \omega \frac{M_2}{M_1 + M_2} \left(\frac{G(M_1 + M_2)P_{orb}^2}{4\pi^2} \right)^{(1/3)} \tag{25}$$

where ω is the angular velocity of the system and K_1 is the radial velocity of the primary. Using $K_1 = 43 \pm 7$ km/s and $M_1 = 0.84 \pm 0.04\ M_\odot$ from the magnesium absorption results in $M_2 = 0.066 \pm 0.013\ M_\odot$ and $q = 0.08 \pm 0.02$. The secondary mass and mass-ratio acquired can be compared against an empirical method derived by Patterson et al. (2005).

$$\epsilon = 0.18q + 0.29q^2 \tag{26}$$

where $\epsilon = (P_{sh} - P_{orb})/P_{orb}$ is the superhump excess. The superhump period was recorded by Kato et al. (2013) to be $P_{sh} = 0.05500 \pm 0.000008$ d. Combined with orbital period by Uthas et al. (2012) $P_{orb} = 0.05432392 \pm 0.00000002$ d resulting superhump excess is $\epsilon = 0.01245 \pm 0.00015$, which with equation 26 results to a mass ratio $q = 0.0628 \pm 0.0007$. From the mass ratio and the white dwarf mass, the mass of the secondary can be determined, giving $M_2 = 0.053 \pm 0.003\ M_\odot$. This value falls in the error margin of the mass estimate $M_2 = 0.066 \pm 0.013\ M_\odot$.

13.4 Semi-Major Axis and Radial Velocity

With the masses of the primary and the secondary known we can calculate the semi-major axis of the system. Using the values $M_1 = 0.84 \pm 0.04\ M_\odot$, $M_2 = 0.066 \pm 0.013\ M_\odot$ and $P_{orb} = 0.05432392 \pm 0.00000002$ d with equation 6 we get $a = 4.06 \times 10^8 \pm 0.07 \times 10^8$ m. Assuming circular orbits results in $K_2 = 504 \pm 12$ km/s.

14 Accretion Disc Parameters

Emission line profiles can be used to determine physical parameters of the accretion disc. Model by Borisov & Neustroev (1997) assumes local line emissivity $f(r) \propto r^{-\alpha}$. Free parameters in the model are: a) Parameter α; b) $R = R_{in}/R_{out}$, the ratio of inner radius to outer radius of the disc; c) V, radial velocity at the outer edge of the disc. Figure 25 shows the effect of each these parameters on the emission line profile.

Higher energy emission lines track hotter areas in the accretion disc. Since inner parts of the disc are hotter, these lines can in theory describe these areas better. Higher energy lines have an intrinsic problem of having lower signal-to-noise ratio though.

Spectra from X-shooter, EFOSC2 and UVES were fitted with white dwarf models with different temperatures, and the best fit was used to remove the white dwarf emission from the spectra. These reduced spectra were then used for emission line profile fitting. In some lines the middle part was left out of the fitting process in order to achieve better fit for the wings. Table 2 contains values for the parameters derived by the model and Figures 26-28 contain the fits themselves.

Table 2: Values of accretion disc parameters determined for each emission line from each dataset.

Set	Line	σ	α	R	V $\times$ sin(i)
UVES	Hα	2.14	0.80	0.09	720
	Hβ	2.98	1.19	0.06	710
	Hγ	3.97	0.95	0.15	720
X-shooter	Hα	0.97	0.42	0.12	760
	Hβ	1.54	0.65	0.05	770
	Hγ	2.31	1.17	0.21	720
	Hδ	3.09	0.74	0.14	740
	Hϵ	3.02	0.92	0.14	760
	Hζ	4.46	-0.02	0.18	780
EFOSC2	Hα	1.82	1.31	0.19	700
	Hβ	3.88	1.59	0.19	680

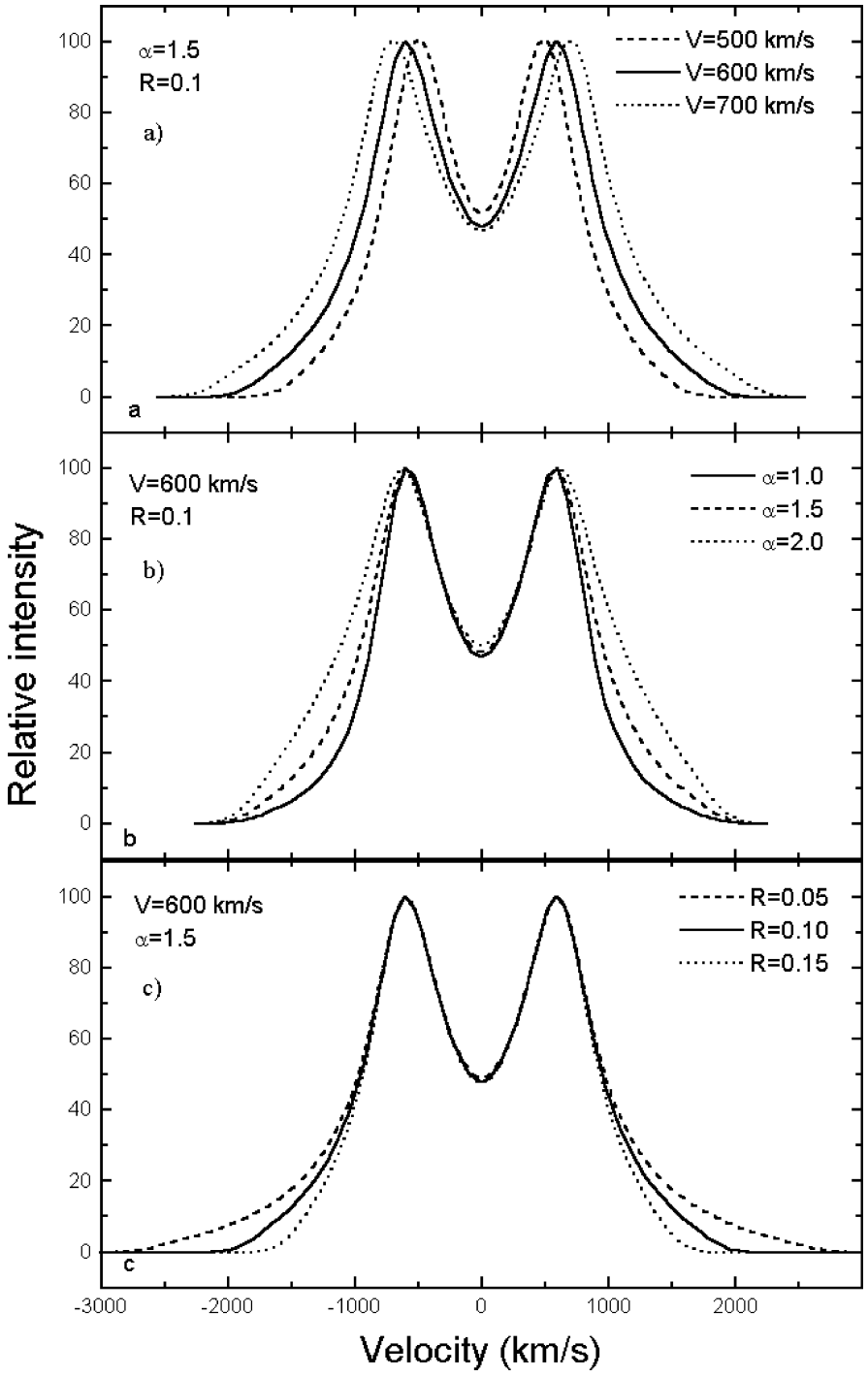

Figure 25: Modelled emission line profile's dependence on model parameters. From Borisov & Neustroev (1997).

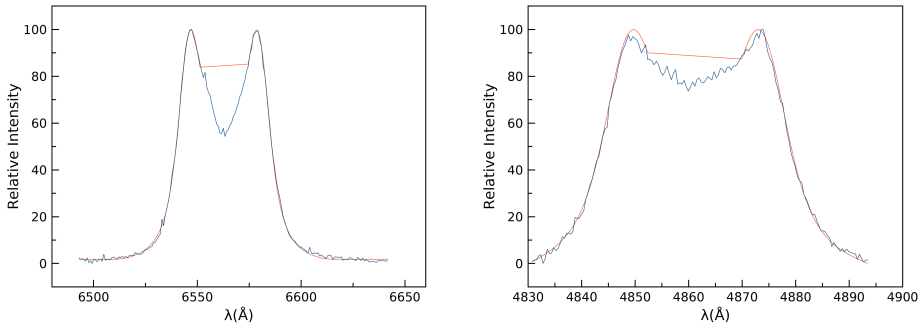

(a) Hα (b) Hβ

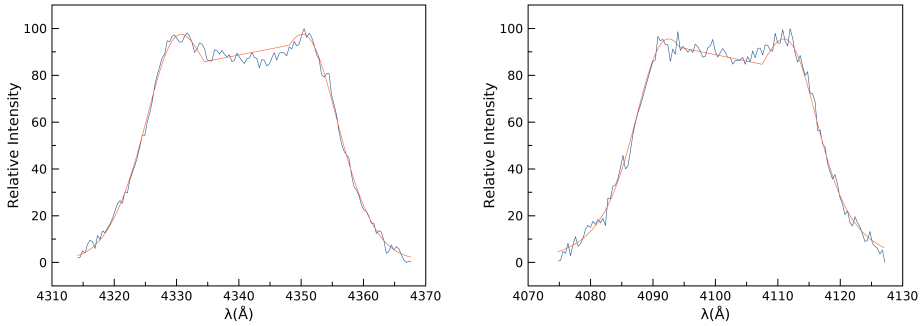

(c) Hγ (d) Hδ

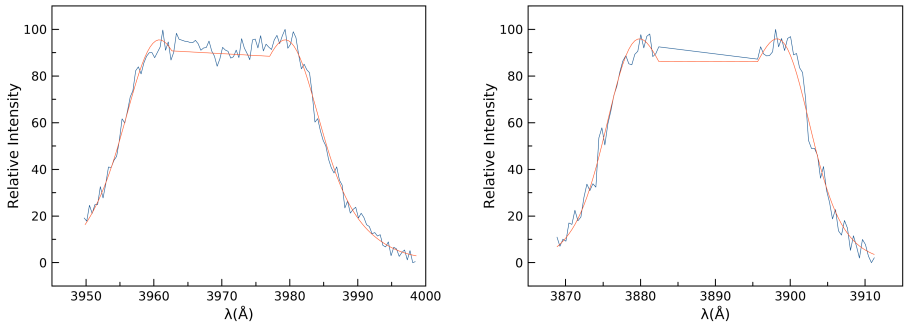

(e) Hϵ (f) Hζ

Figure 26: Several hydrogen emission lines from X-shooter data fitted with the model.

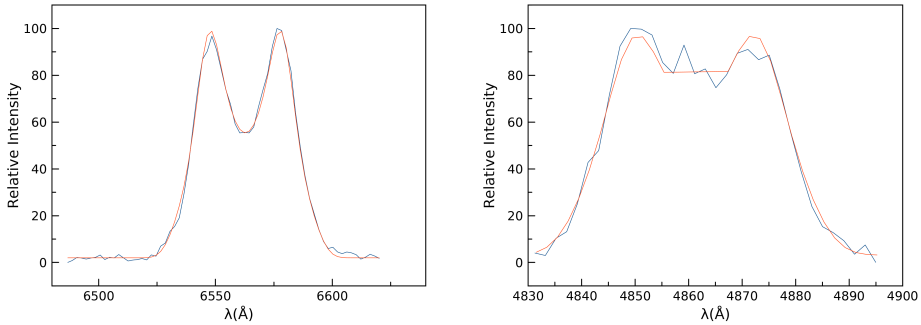

(a) Hα (b) Hβ

Figure 27: Two hydrogen emission lines from EFOSC2 data fitted with the model.

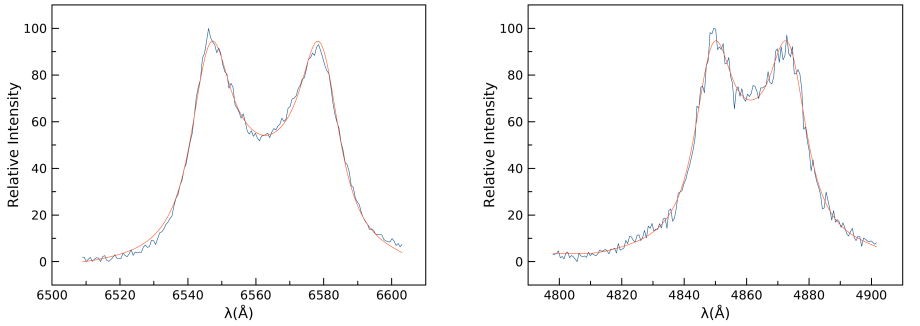

(a) Hα (b) Hβ

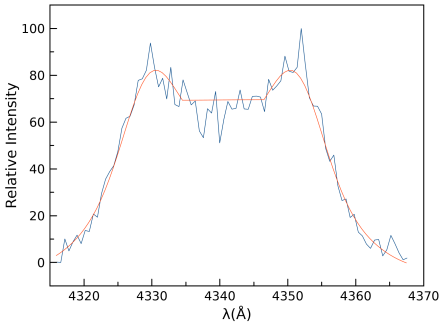

(c) Hγ

Figure 28: Three hydrogen emission lines from UVES data fitted with the model.

15 Doppler Tomography

15.1 Overview

Doppler tomography of binary stars is based on the assumption that the object doesn't change much in the duration of a single rotation. Time resolved spectra taken during different orbital phases can be equivalently thought in two ways. Firstly by having the observer at rest, and the object rotates. Or second, by having the object at rest, and the observer measures the spectra from different viewing directions. The latter approach may be unintuitive at first, but can be beneficial when discussing tomography.

Tomography is the inversion of projections to construct the original image. Doppler tomography therefore is using the spectral Doppler shifts to reconstruct the image. This reconstructed image is in velocity coordinates, which don't uniquely map to spatial coordinates, unless significant assumptions are made. For instance Keplerian orbits of individual particles, which is shown in Figure 29.

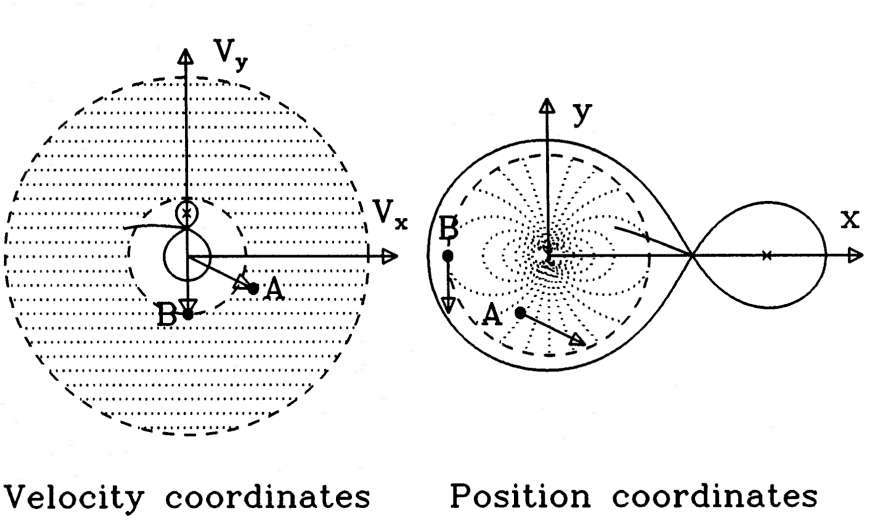

Figure 29: Connection between spatial and velocity coordinates in Keplerian velocity distribution. From Marsh & Horne (1988).

15.2 Profile Projection

When defining velocity coordinates one needs to take care to define velocities in inertial coordinates rather than in rotating coordinates. In CVs the inertial frame is conventionally defined so that the x-axis points from the white dwarf to the secondary, and the y-axis in the direction of the motion of the secondary, from the white dwarf.

Any point in the velocity space produces radial velocity according to equation 27, where γ is the systemic velocity of the system, and ϕ is the orbital phase of the system. Thus the spectra of the system can be projected by integrating this equation for all velocities at any phase. This integral is in equation 28, where $g(V - V_R)$ describes the line profile of each point and the instrumental blurring.

$$V_R = \gamma - V_x \cos 2\pi\phi + V_y \sin 2\pi\phi \tag{27}$$

$$f(V, \phi) = \int_{-\infty}^{\infty} \int_{-\infty}^{\infty} I(V_x, V_y) g(V - V_R) dV_x dV_y \tag{28}$$

15.3 Maximum Entropy Inversion

More difficult and scientifically interesting case is the reverse process from what was just described, constructing the velocity space image from spectra taken at different orbital phases. One way to perform this is so called maximum entropy inversion method. In this method an image with maximum entropy is selected:

$$S = -\sum_{i=1}^{M} p_i \ln \frac{p_i}{q_i} \tag{29}$$

Here:

$$q_i = \frac{D_i}{\sum_{j=1}^{M} D_j}, p_i = \frac{I_i}{\sum_{j=1}^{M} I_j} \tag{30}$$

Where D is the default image, and I is the constructed image. This entropy measures difference between the original image, and the reconstructed image. By good initial guess and iterative process the Doppler map can be constructed. We used the code developed by Spruit (1998).

15.4 Doppler maps of BW Scl

In Figures 30-32 are the spectra and the Doppler maps of BW Scl in Hα, the rest are in appendix A. The first subfigure (a) contains the original measured spectra, compiled by phases. The second subfigure (b) contains reconstructed spectra compiled by phases. The reconstructed spectra is a projected profile of the constructed Doppler map, and is a good measure on the validity of the Doppler map. The original measured spectra and the reconstructed spectra should be similar for a good Doppler map. Finally in subfigure (c) we have the Doppler map itself. For aforementioned reasons the map is in velocity coordinates, with the primary at the origin. The secondary is above the primary. Lines drawn from the secondary represent the gas stream, which is drawn twice. Once for the velocity of the gas falling from the inner Lagrangian point and once for the Keplerian velocity along this path. These lines act as limiting values for the gas stream. Since the map is in velocity coordinates, the disc is "turned inside out". Radial velocities are largest near the primary in spatial coordinates, thus they are plotted furthest from it in velocity coordinates.

The Doppler maps show that the accretion disc is dominated by the bright spot, which is found in the expected position. The maps also reveal a consistent emission structure around $\sim 135°$. This structure is present in all datasets, and is more prominent in higher order Balmer lines. The accretion disc is not visible in any helium emission lines.

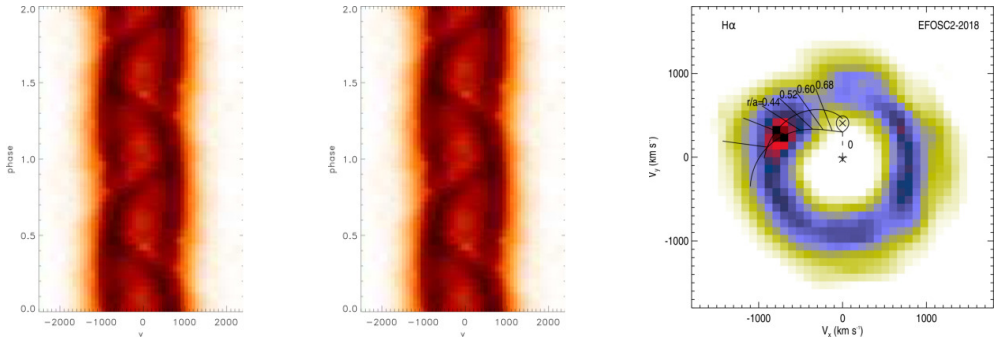

(a) (b) (c)

Figure 30: a) Trailed spectra b) reconstructed spectra c) Doppler map of Hα from the EFOSC2 data.

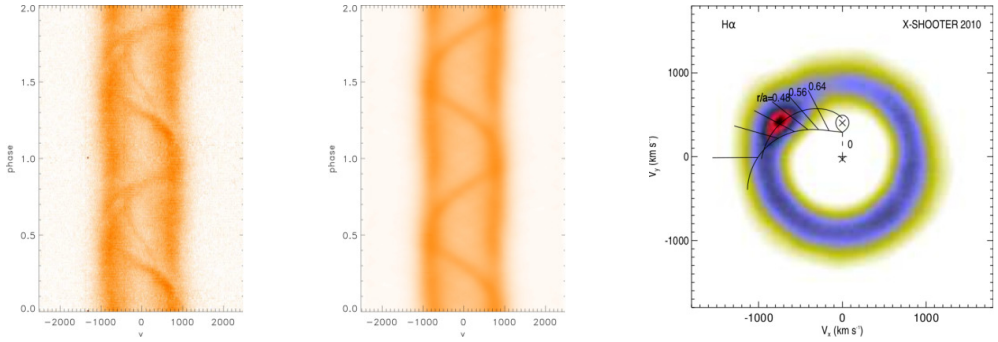

(a) (b) (c)

Figure 31: a) Trailed spectra b) reconstructed spectra c) Doppler map of Hα from the X-shooter data. Note the additional smaller amplitude sinusoidal component in the trailed spectra.

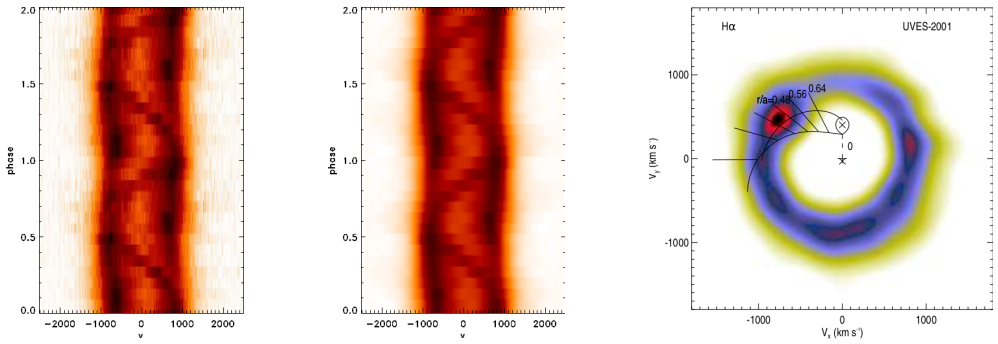

(a) (b) (c)

Figure 32: a) Trailed spectra b) reconstructed spectra c) Doppler map of Hα from the UVES data.

16 Direct Measurements of the Secondary

16.1 Hα Emission

Trailed spectra of Hα from the X-shooter data in Figure 31 reveals a sinusoidal signal with amplitude ∼400 km/s. This signal is only present in phases 0.3-0.8. The signal is not present in the reconstructed spectra, implying that the source is not represented in the Doppler map. The amplitude corresponds to the radial velocity of the secondary, $K_2 \approx 500$ km/s, though a bit lower. The source is most likely the side of the secondary which is facing towards the WD and is heated up by it. Since the secondary's shape follows its Roche-lobe, it is highly distorted and the radial velocity amplitude is lower than that of the secondary's center of mass. This theory is further reinforced by the signal being present only in phases 0.3-0.8, as the heated up face is visible only in part of the orbit.

Calculating the Doppler map with only phases 0.3-0.8 selected enables the program to locate the source on the map. The result is in Figure 33. The Doppler map shows a region of emission coinciding with the secondary.

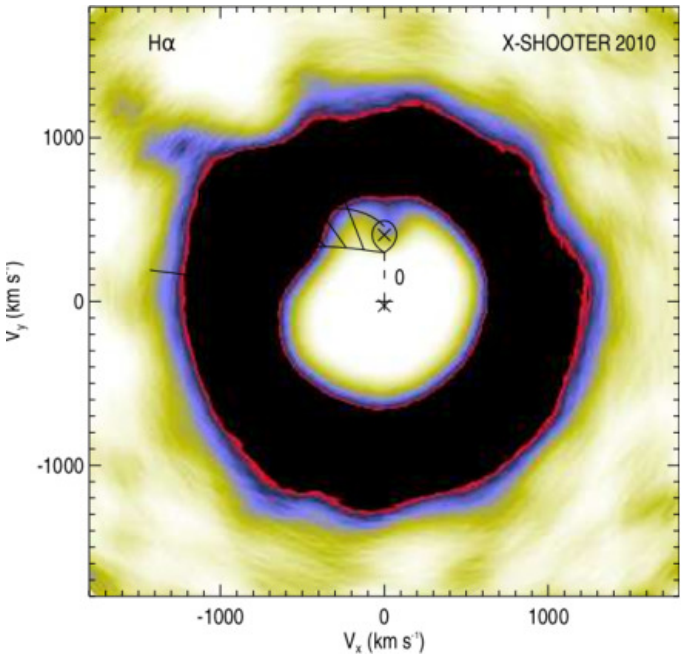

Figure 33: Doppler map of Hα, with only phases 0.3-0.8 present. Contrast has been increased to reveal the secondary.

For further analysis of the signal, the X-shooter spectra were binned in

40 phase bins, and the signal was fitted with a Gaussian function using `IRAF`. The center of the Gaussian as a function of the phase was then fitted with a sine function, resulting in amplitude of 463 ± 13 km/s.

16.2 The "K-correction"

In systems where the secondary is significantly irradiated by the primary, the observed velocity amplitude can be distorted. This distortion is caused by a non-uniform distribution of emission from the heated-up face of the secondary. The observed centre-of-light can thus be significantly different from the center of mass of the secondary. This can be remedied by applying a "K-correction" shown in equation 31 by Wade & Horne (1988), see also Warner (1995).

$$\frac{K_{2,o}}{K_2} \approx 1 - 0.462 q^{1/3} (1+q)^{2/3} \frac{\Delta R_2}{R_2} \tag{31}$$

Here $K_{2,o}$ is the observed radial velocity, K_2 is the radial velocity of the center of mass, and ratio $\frac{\Delta R_2}{R_2}$ describes the distribution of emission from the secondary. $\frac{\Delta R_2}{R_2} = 1$ corresponds to all light originating from the L1, 0.5 corresponds to the light coming from the half sphere illuminated by the primary, and 0 correspond to perfect symmetry. Using values $q = 0.08 \pm 0.02$, $K_{2,o} = 463 \pm 13$ km/s and $\frac{\Delta R_2}{R_2} = 0.5$ we get $K_2 = 517 \pm 20$ km/s.

16.3 Calcium Emission

In Figures 34 and 35 are the trailed spectra, reconstructed spectra and Doppler maps of the Ca II emission lines at 8498.02 Å and 8542.09 Å. Both Doppler maps identify a source of radiation coinciding with the secondary. In both maps the telluric lines produce circular artifacts at low and high velocities. Similarly to Hα emission from the secondary, the emission is visible in the trailed spectra only in phases $\sim 0.3 - 0.8$.

In Figure 36 are the trailed spectra, reconstructed spectra and Doppler maps of the Ca II emission line at 3933.664 Å. Unlike the Ca II emission lines at IR, the emission source coincides with the bright spot, rather than with the secondary. This is consistent with the trailed spectra, since its amplitude is roughly double of that in Figures 34 and 35. The emission line is also visible in all phases.

The secondary being visible in the Doppler maps of Ca II emission lines allows for an accurate estimation of the zero phase of the system. From this we can deduce a new estimate for the ephemeris of the system
HJD $= 2450032.188 \pm 0.003 + 0.05432392 \pm 0.00000002$.

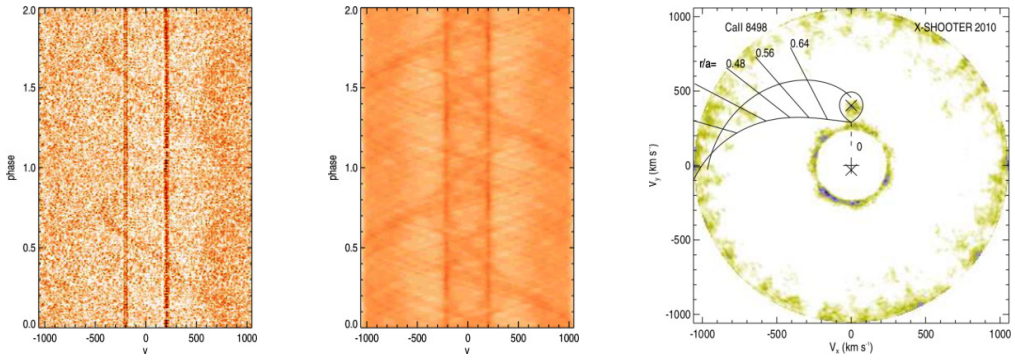

(a) (b) (c)

Figure 34: a) Trailed spectra b) reconstructed spectra c) Doppler map of Ca II at 8498 Å from the X-shooter data.

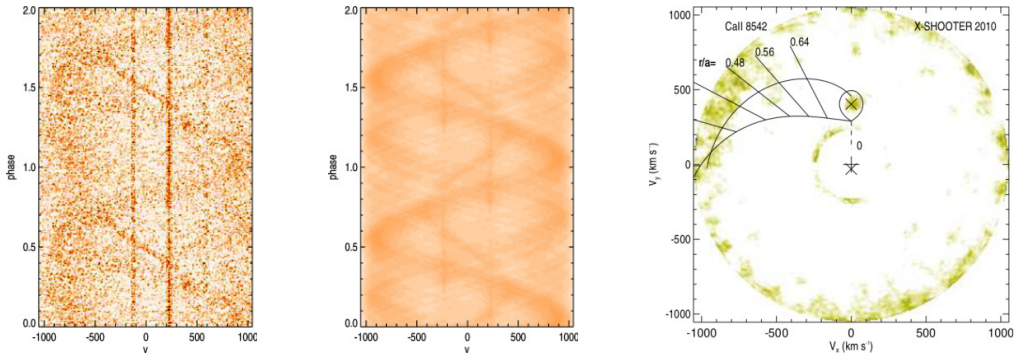

(a) (b) (c)

Figure 35: a) Trailed spectra b) reconstructed spectra c) Doppler map of Ca II at 8542 Å from the X-shooter data.

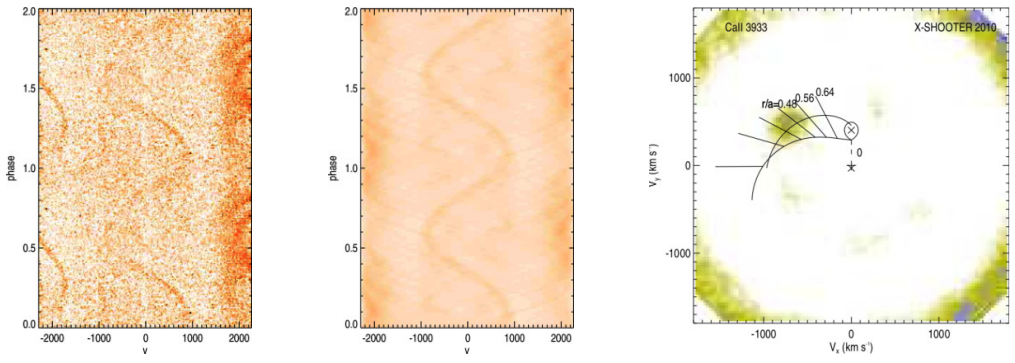

(a) (b) (c)

Figure 36: a) Trailed spectra b) reconstructed spectra c) Doppler map of Ca II at 3933 Å from the X-shooter data.

17 Conclusion

In this thesis we present radial velocity analysis, Doppler tomography and emission profile fitting for the period-bouncer candidate BW Sculptoris, from data obtained in 2001, 2002, 2010, 2018. In the middle of these observation in 2011, BW Scl went through its first and only superoutburst. All the spectra of the object are dominated by strong double-peaked Balmer emission lines from the accretion disc, which sit in broad absorption troughs originating from the white dwarf. Other weaker emission lines such as helium and calcium are also present, and most importantly the Mg II absorption line at 4481 Å.

Based on the Mg II line we estimate the surface gravity of the primary and conclude that $M_1 = 0.84 \pm 0.04\ M_\odot$, which is very typical for a CV white dwarf. From the Mg II line we also estimate that $K_1 = 43 \pm 7$ km/s. From these values we derive $M_2 = 0.066 \pm 0.013\ M_\odot$ and $q = 0.08 \pm 0.02$. Thus we come to the conclusion that the secondary star in BW Scl is a brown dwarf.

Radial velocity analysis affirms the ∼40 km/s radial velocity for the primary, and the almost zero system velocity. Our analysis also finds the phase difference between photometric maximum and the inferior conjunction to be $\phi \approx 0.15$.

The emission profile fitting suggests that the accretion disc is at its smallest extent before the superoutburst (X-shooter data) with $V \times \sin(i) \approx 750$ km/s, which then expands to $V \times \sin(i) \approx 700$ km/s (EFOSC2 data). Our analysis also suggests that the accretion disc changes closer to a ring like structure after the outburst. $R_{in}/R_{out} \approx 0.10$ in UVES and X-shooter data, whereas $R_{in}/R_{out} = 0.19$ in UVES data. The profile fitting suggests that the inclination in BW Scl is very high, almost eclipsing. No eclipses are observed however. This result is further supported by the Doppler maps, where the secondary is visible.

Finally the Doppler tomography displays consistent emission structure around $\sim 135°$ measured from the bright spot. This structure is present in all datasets, and is more prominent in higher order Balmer lines. This structure has been observed in many other CVs (e.g. Neustroev et al. 2016). We are also able to directly observe the secondary in Hα and Ca II.

Because of the near period-minimum P_{orb}, and $M_2 < 0.08$ for the secondary, we come to the conclusion that BW Scl is a period-bouncer.

18 Acknowledgements

We acknowledge with thanks the variable star observations from the AAVSO International Database contributed by observers worldwide and used in this research.
This work has made use of data from the European Space Agency (ESA) mission *Gaia* (`https://www.cosmos.esa.int/gaia`), processed by the *Gaia* Data Processing and Analysis Consortium (DPAC, `https://www.cosmos.esa.int/web/gaia/dpac/consortium`). Funding for the DPAC has been provided by national institutions, in particular the institutions participating in the *Gaia* Multilateral Agreement.

References

AAVSO. 2019, American Association of Variable Star Observers, https://www.aavso.org/, accessed: 2019-7-4

Abbott, T. M. C., Fleming, T. A., & Pasquini, L. 1997, Astronomy and Astrophysics, 318, 134

Augusteijn, T. & Wisotzki, L. 1997, Astronomy and Astrophysics, 324, L57

Bath, G. T. & Pringle, J. E. 1982, Monthly Notices of the RAS, 201, 345

Borisov, N. V. & Neustroev, V. V. 1997, Bulletin of the Special Astrophysics Observatory, 44, 110

Buzzoni, B., Delabre, B., Dekker, H., et al. 1984, The Messenger, 38, 9

Chandrasekhar, S. 1939, Ciel et Terre, 55, 412

Dekker, H., D'Odorico, S., Kaufer, A., Delabre, B., & Kotzlowski, H. 2000, in Society of Photo-Optical Instrumentation Engineers (SPIE) Conference Series, Vol. 4008, Optical and IR Telescope Instrumentation and Detectors, ed. M. Iye & A. F. Moorwood, 534–545

Frank, J., King, A. R., & Raine, D. J. 1985, Accretion power in astrophysics

Freudling, W., Romaniello, M., Bramich, D. M., et al. 2013, Astronomy and Astrophysics, 559, A96

Gaia Collaboration, Brown, A. G. A., Vallenari, A., et al. 2018, Astronomy and Astrophysics, 616, A1

Gaia Collaboration, Prusti, T., de Bruijne, J. H. J., et al. 2016, Astronomy and Astrophysics, 595, A1

Gänsicke, B. T., Szkody, P., Howell, S. B., & Sion, E. M. 2005, Astrophysical Journal, 629, 451

Goliasch, J. & Nelson, L. 2015, Astrophysical Journal, 809, 80

Greenstein, J. L. & Trimble, V. L. 1967, Astrophysical Journal, 149, 283

Hamada, T. & Salpeter, E. E. 1961, Astrophysical Journal, 134, 683

Hellier, C. 2001, Cataclysmic Variable Stars

Horne, K. & Marsh, T. R. 1986, Monthly Notices of the Royal Astronomical Society, 218, 761

Hōshi, R. 1979, Progress of Theoretical Physics, 61, 1307

Ichikawa, S., Hirose, M., & Osaki, Y. 1993, Publications of the ASJ, 45, 243

Kato, T., Hambsch, F.-J., Maehara, H., et al. 2013, Publications of the ASJ, 65, 23

Kawaler, S. D. 1988, Astrophysical Journal, 333, 236

Kimura, M., Isogai, K., Kato, T., et al. 2018, Publications of the ASJ, 70, 47

Knigge, C. 2006, Monthly Notices of the Royal Astronomical Society, 373, 484

La Dous, C. 1989, Astronomy and Astrophysics, 211, 131

Landau, L., Lifshitz, E., & Rarita, W. 1952, Physics Today, 5, 25

Lubow, S. H. & Shu, F. H. 1976, Astrophysical Journal, Letters, 207, L53

Marsh, T. R. & Horne, K. 1988, Monthly Notices of the Royal Astronomical Society, 235, 269

Mennickent, R. E., Diaz, M. P., & Tappert, C. 2004, Monthly Notices of the RAS, 347, 1180

Neustroev, V. V. & Zharikov, S. V. 2020, Astronomy and Astrophysics, 642, A100

Neustroev, V. V., Zharikov, S. V., & Borisov, N. V. 2016, Astronomy and Astrophysics, 586, A10

Osaki, Y. 1974, Publications of the ASJ, 26, 429

Paczyński, B. 1971, Annual Review of Astronomy and Astrophysics, 9, 183

Paczynski, B. 1977, Astrophysical Journal, 216, 822

Pala, A. F. & Gänsicke, B. T. 2017, in Astronomical Society of the Pacific Conference Series, Vol. 509, 20th European White Dwarf Workshop, ed. P. E. Tremblay, B. Gaensicke, & T. Marsh, 91

Pala, A. F., Gänsicke, B. T., Marsh, T. R., et al. 2019, Monthly Notices of the Royal Astronomical Society, 483, 1080

Patterson, J. 2011, Monthly Notices of the Royal Astronomical Society, 411, 2695

Patterson, J., Kemp, J., Harvey, D. A., et al. 2005, Publications of the Astronomical Society of the Pacific, 117, 1204

Pojmanski, G. 1986, Acta Astronomica, 36, 69

Pringle, J. & Wade, R. 1985, Interacting binaries, Vol. 150 (Cambridge University Press)

Shafter, A. W. 1983, Astrophysical Journal, 267, 222

Spruit, H. C. 1998, arXiv e-prints, astro

Tody, D. 1986, in Society of Photo-Optical Instrumentation Engineers (SPIE) Conference Series, Vol. 627, Instrumentation in astronomy VI, ed. D. L. Crawford, 733

Uthas, H., Patterson, J., Kemp, J., et al. 2012, Monthly Notices of the Royal Astronomical Society, 420, 379

Vernet, J., Dekker, H., D'Odorico, S., et al. 2011, Astronomy and Astrophysics, 536, A105

Wade, R. A. & Horne, K. 1988, Astrophysical Journal, 324, 411

Warner, B. 1995, Cataclysmic Variable Stars, Cambridge Astrophysics (Cambridge University Press)

Young, P. & Schneider, D. P. 1980, Astrophysical Journal, 238, 955

Appendix A

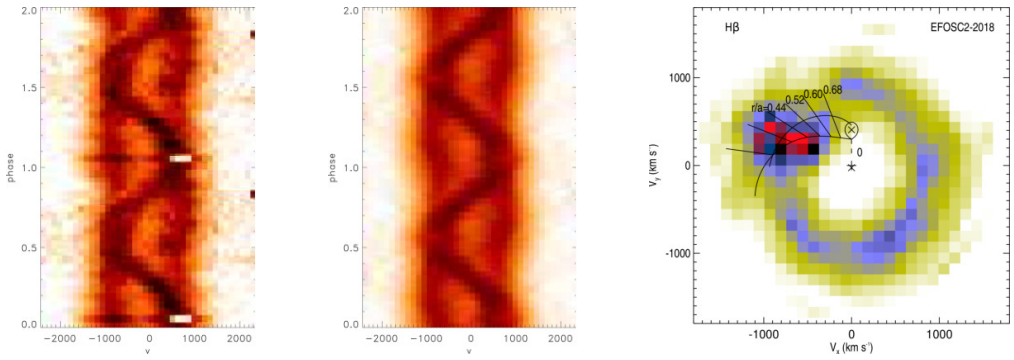

(a) (b) (c)

Figure 37: a) Trailed spectra b) reconstructed spectra c) Doppler map of Hβ from EFOSC2 data.

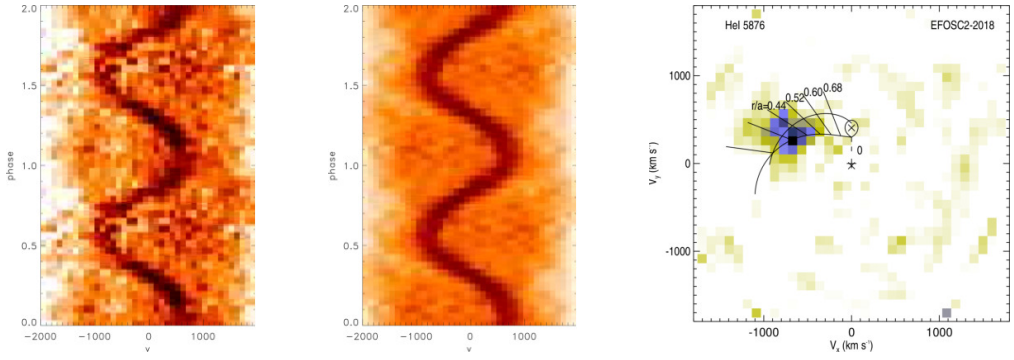

(a) (b) (c)

Figure 38: a) Trailed spectra b) reconstructed spectra c) Doppler map of He5875 from EFOSC2 data.

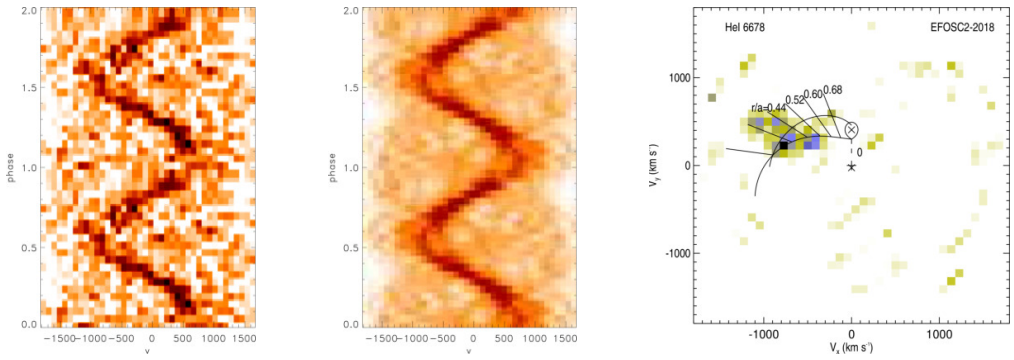

(a) (b) (c)

Figure 39: a) Trailed spectra b) reconstructed spectra c) Doppler map of He6678 from EFOSC2 data.

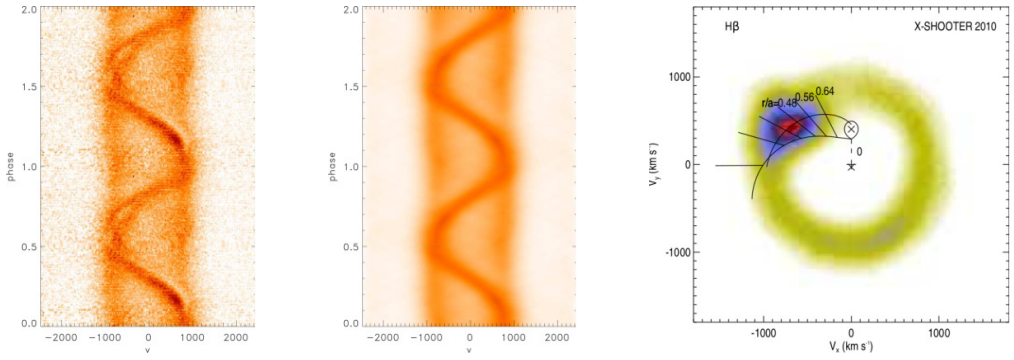

(a) (b) (c)

Figure 40: a) Trailed spectra b) reconstructed spectra c) Doppler map of Hβ from X-shooter data.

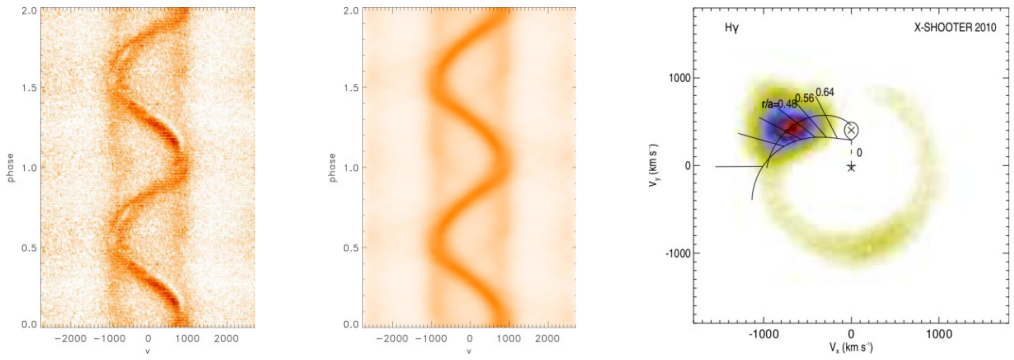

(a) (b) (c)

Figure 41: a) Trailed spectra b) reconstructed spectra c) Doppler map of Hγ from X-shooter data.

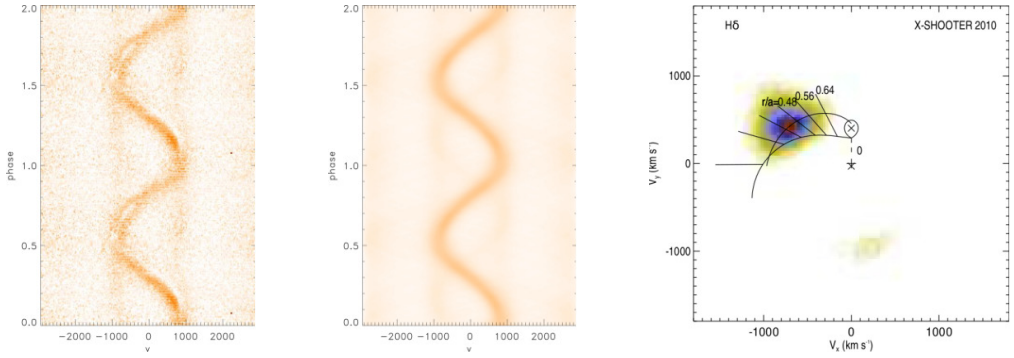

(a) (b) (c)

Figure 42: a) Trailed spectra b) reconstructed spectra c) Doppler map of Hδ from X-shooter data.

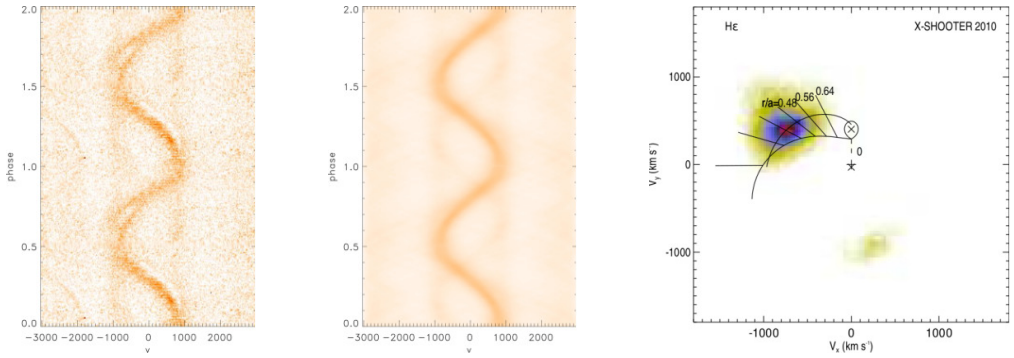

(a) (b) (c)

Figure 43: a) Trailed spectra b) reconstructed spectra c) Doppler map of Hϵ from X-shooter data.

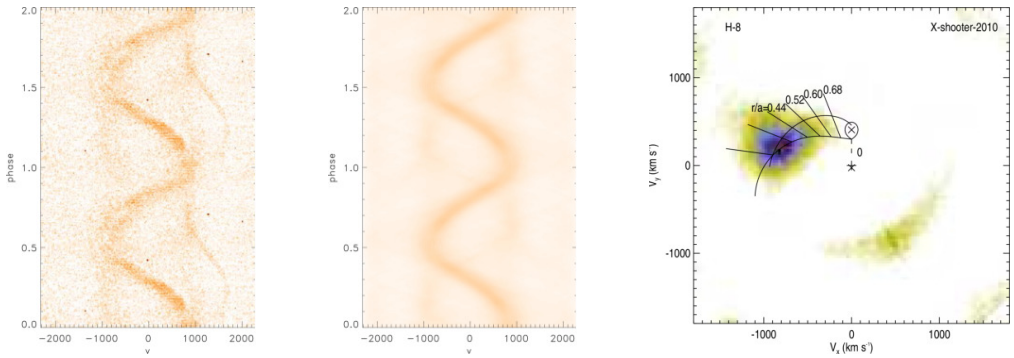

(a) (b) (c)

Figure 44: a) Trailed spectra b) reconstructed spectra c) Doppler map of Hζ from X-shooter data.

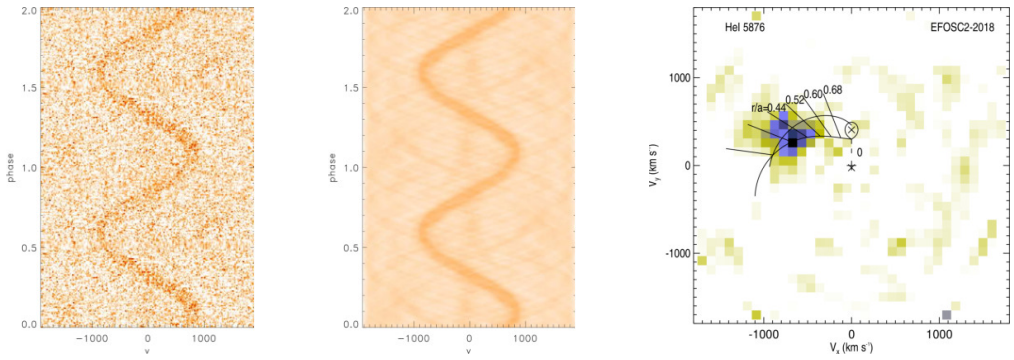

(a) (b) (c)

Figure 45: a) Trailed spectra b) reconstructed spectra c) Doppler map of He4686 from X-shooter data.

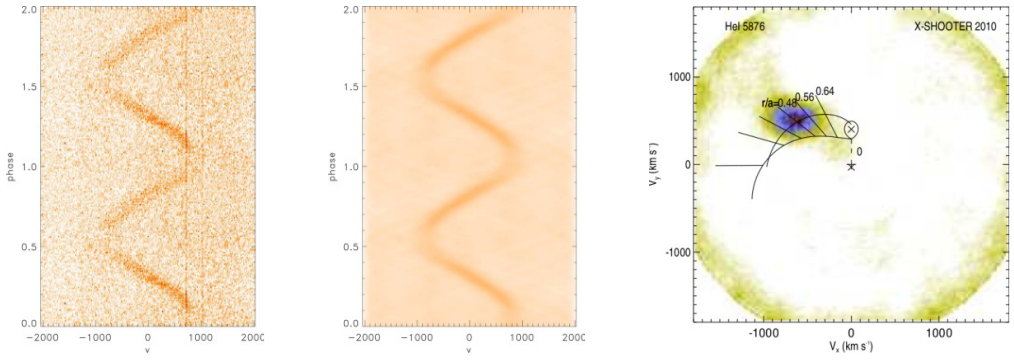

(a) (b) (c)

Figure 46: a) Trailed spectra b) reconstructed spectra c) Doppler map of He5875 from X-shooter data.

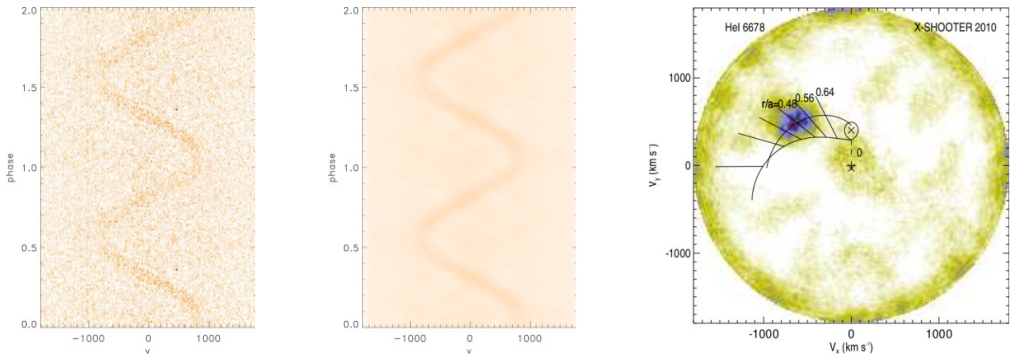

(a) (b) (c)

Figure 47: a) Trailed spectra b) reconstructed spectra c) Doppler map of He6678 from X-shooter data.

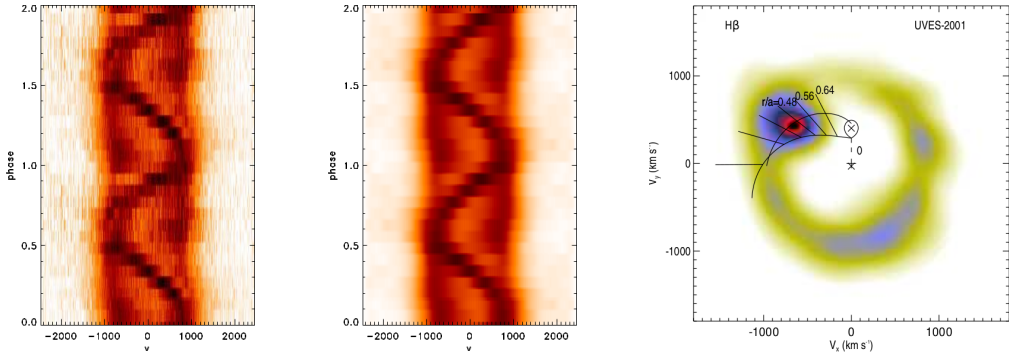

(a) (b) (c)

Figure 48: a) Trailed spectra b) reconstructed spectra c) Doppler map of Hβ from UVES data.

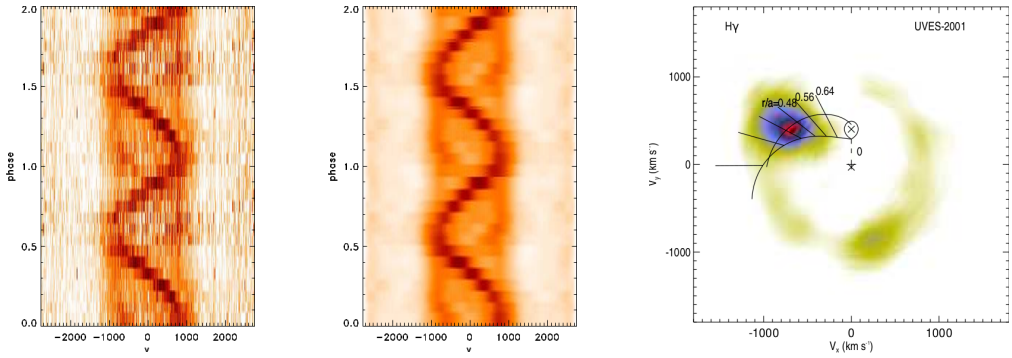

(a) (b) (c)

Figure 49: a) Trailed spectra b) reconstructed spectra c) Doppler map of Hγ from UVES data.

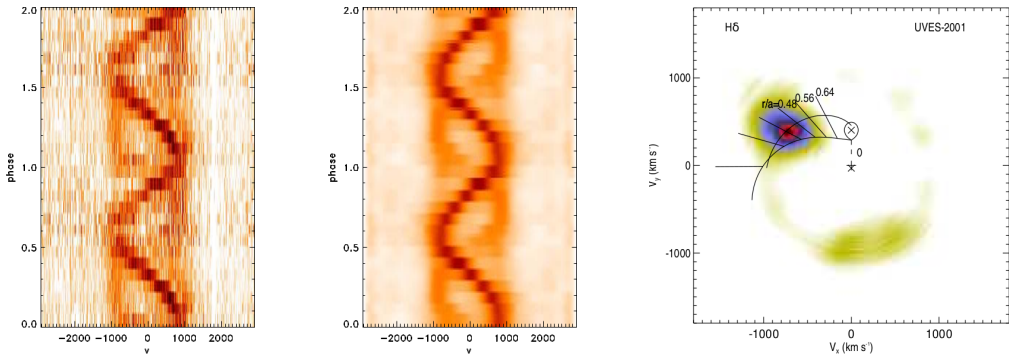

(a) (b) (c)

Figure 50: a) Trailed spectra b) reconstructed spectra c) Doppler map of Hδ from UVES data.

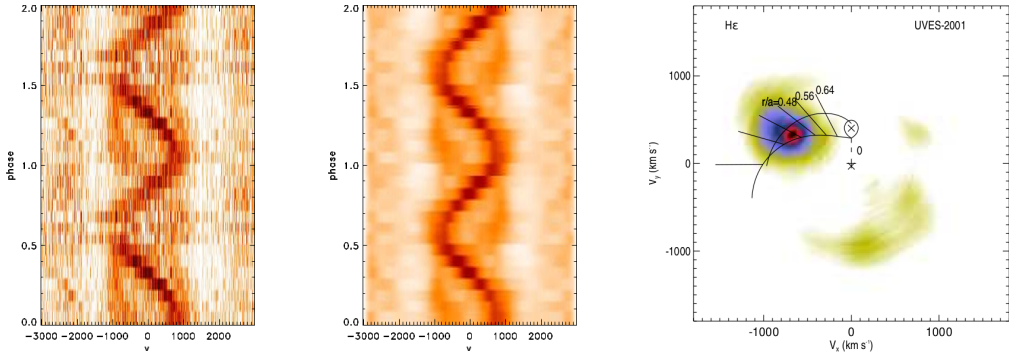

(a) (b) (c)

Figure 51: a) Trailed spectra b) reconstructed spectra c) Doppler map of Hϵ from UVES data.

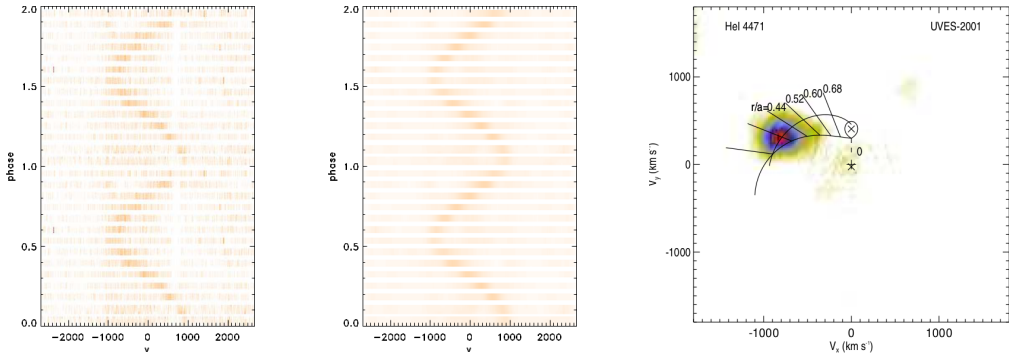

(a) (b) (c)

Figure 52: a) Trailed spectra b) reconstructed spectra c) Doppler map of He4471 from UVES data.

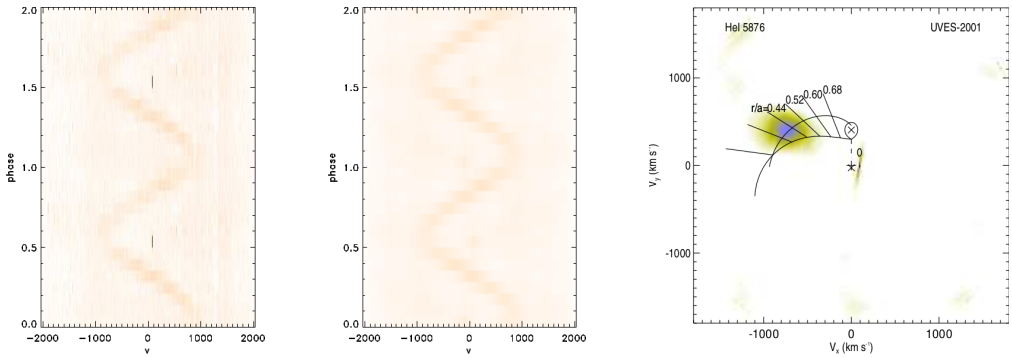

(a) (b) (c)

Figure 53: a) Trailed spectra b) reconstructed spectra c) Doppler map of He5875 from UVES data.